Reusable Launchers: Development of a Coupled Flight Mechanics, Guidance and Control Benchmark

Pedro Simplício* and Andrés Marcos†
University of Bristol, BS8 1TR Bristol, United Kingdom

Samir Bennani‡
European Space Agency, 2201 AZ Noordwijk, The Netherlands

This article studies the mechanics of reusable retro-propelled flight of slender low lift-to-drag bodies via integrated guidance and control simulations. To do this, a simulation benchmark focused on the coupling between flight mechanics, guidance and control must be developed, as opposed to mission-optimisation oriented ones that simplify (or directly ignore) these couplings. The developed simulator covers vertical take-off and landing of a first stage booster for return to launch site and downrange landing missions. In order to steer it towards a controlled entry, followed by descent and precision landing, the vehicle is configured with a deep throttling thrust vector control system, fins and cold gas thrusters. Comparative performance results are derived in terms of aerodynamic loads and heat fluxes for both recovery scenarios, as well as through a detailed closed-loop controllability analysis. The latter demonstrates that the configuration has sufficient authority and resolution to perform stable flight and adequate wind gust rejection. The developed benchmark (because of the coupled flight mechanics, guidance and control) allows to provide a first assessment of operational limits, as well as mission and GNC specifications. This in turn paves the way for the synthesis and assessment of more sophisticated reusable launcher guidance and control algorithms.

I. Introduction

The potential benefits and technical feasibility of launcher reusability as a key paradigm for sustainable access to space have been recently demonstrated by private companies (i.e. SpaceX and Blue Origin with the successful vertical take-off and vertical landing (VTVL) of reusable boosters [1]). In parallel, several programmes and studies have been established to study and further reusability. Most of these studies [2–6] are focused on the application of a multi-disciplinary optimisation (MDO) framework to determine combined launch and recovery (L&R) reference trajectories, staging conditions and vehicle configurations that allow to reach the highest payload while keeping

*PhD Candidate, Aerospace Engineering Department, University Walk.
†Senior Lecturer, Aerospace Engineering Department, University Walk. Senior Member AIAA.
‡GNC Launcher Systems Expert, ESTEC GNC Section, Keplerlaan 1. Senior Member AIAA

aerodynamic and thermal loads at reasonable levels. Although the MDO approach is extremely valuable for preliminary system sizing, it is not well suited to study the existing couplings between flight mechanics, guidance and control (G&C).

In complement to these efforts, an European Space Agency sponsored activity is studying other efficient design frameworks to manage the aforementioned requirements through closed-loop recovery guidance algorithms and robust attitude control with active load relief capabilities. However, these techniques require a deeper understanding of reusable flight mechanics and of its couplings with G&C algorithms and mechanisms than what is considered within the MDO framework. This becomes even more relevant for the next-generation of launchers, where more flexible structures lead to stronger aeroelastic couplings between control-induced loads, wind perturbations and rigid-body motion [7, 8]. Hence, in order to carry out the activity, a nonlinear 6 degrees-of-freedom benchmark model for the integrated assessment of reusable launcher G&C approaches is developed in this article.

The benchmark simulates the L&R trajectory of a mixed-fuel VTVL booster used as first stage of a lightweight, non-winged launcher injecting a 1,100 kg satellite in a quasi-polar orbit at 800 km. It is noted that the goal of this work is not to provide a high-level fidelity industrial simulator, but to show how a reusable launcher benchmark can be built. The representativeness of the modelling simplifications (e.g. constant specific impulse throughout the flight) are tailored to the aforementioned aim of coupled flight mechanics and G&C studies, and configuration parameters (as well as G&C algorithms) can be easily modified and assessed thanks to its modular architecture. Indeed, this modularity has been used in reference [9] to develop and verify an on-board convex optimisation-based guidance algorithm termed *DESCENDO* (Descending over Extended Envelopes using Successive Convexification-based Optimisation).

The layout of this article begins in Sec. II with the description of all the building blocks of the model: from reference frames, environment models, and aerodynamics/thermal properties to mass, centre of gravity and inertia calculations. Then, the L&R mission scenarios under assessment are introduced in Sec. III, as well as a simple closed-loop guidance law employed as baseline for retro-propulsive entry, descent and pinpoint landing. Two recovery scenarios are addressed: downrange landing (DRL), in which the reusable stage lands close to its un-propelled impact site, and return to launch site (RTLS), where the stage uses an additional firing to return to launch site. In addition, Sec. IV showcases, using a preliminary control algorithm, the manner attitude control can be designed and integrated in the reusable launch vehicle (RLV) benchmark while taking into account thrust vector control (TVC), fins and cold gas thrusters. Finally, Sec. V presents detailed flight mechanics simulations for both DRL and RTLS missions, as well a preliminary controllability analysis for the former method of recovery.

II. RLV Flight Mechanics Modelling

The reusable launch vehicle (RLV) flight mechanics model developed for this study results from the interconnection of several system building blocks. These elements have been implemented using MATLAB/Simulink and will be presented in the following subsections.

Reference frames and environment models adopted for gravity, atmosphere and wind are described in Sec. II.A. Then, a detailed description of the equations of motion, aerodynamic calculations and mass, CG & inertia (MCI) evolution is provided in Sec. II.B, II.C and II.G, respectively. The vehicle is mainly steered via thrust vector control (TVC), but two pairs of fins are also included to provide attitude control under low thrust, as well as two pairs of cold gas thrusters for pitch and yaw manoeuvring in low dynamic pressure conditions. These actuators are introduced in Sec. II.D, II.E and II.F, respectively.

Finally, guidance and control (G&C) algorithms are organised in three subsystems. The first one, "launch & recovery (L&R) guidance", is responsible for the online generation of thrust and attitude commands. A dedicated discussion on L&R mission profiles and guidance techniques is provided in Sec. III. Then, the "attitude control" subsystem (responsible for the computation of attitude control moments) and the "control allocation" subsystem (for the allocation among the aforementioned actuators) are presented in Sec. IV.

A. Reference Frames & Environment Models

This subsection introduces the reference frames and environment models that are essential to simulate the motion of RLVs during flight. For a thorough description of these frames and their coordinate transformations, the reader is referred to [10] or [11].

The first reference frame is the Earth-Centred Inertial (ECI) frame, with basis vectors $\{\mathbf{i}_\mathrm{I},\, \mathbf{j}_\mathrm{I},\, \mathbf{k}_\mathrm{I}\}$. Its origin is at the centre of the Earth, $\mathbf{i}_\mathrm{I}$ points to the vernal equinox, $\mathbf{k}_\mathrm{I}$ to the North pole and $\mathbf{j}_\mathrm{I}$ completes a right-handed set. Since the Earth's orbital motion around the Sun can be neglected for the study of RLV trajectories, the ECI frame is considered inertial and the equations of motion are referred to it.

With the same origin and equatorial plane, the Earth-Centred Earth-Fixed (ECEF) frame is defined by the set of vectors $\{\mathbf{i}_\mathrm{E},\, \mathbf{j}_\mathrm{E},\, \mathbf{k}_\mathrm{E}\}$. This frame rotates with the Earth's angular velocity $\boldsymbol{\Omega}_\mathrm{I} = \omega_\mathrm{E}\, \mathbf{k}_\mathrm{I}$, keeping $\mathbf{i}_\mathrm{E}$ along the Greenwich meridian. It is useful for the computation of position-dependent quantities due to a straightforward conversion between its coordinates and latitude, longitude and altitude $\{\varphi(t),\, \lambda(t),\, h(t)\}$.

In this study, simulations are initiated from the European Space Centre situated in French Guiana [12], with $\{\varphi(0),\, \lambda(0),\, h(0)\} \approx \{5.2 \text{ deg}, -52.8 \text{ deg}, 0 \text{ m}\}$. Defining this initial position in the ECI frame as $\mathbf{r}_\mathrm{I}(0)$, the initial velocity of the vehicle due to the Earth's rotation is $\mathbf{v}_\mathrm{I}(0) = \boldsymbol{\Omega}_\mathrm{I} \times \mathbf{r}_\mathrm{I}(0)$. Furthermore, the rotation quaternion $\mathbf{q}_\mathrm{E}^\mathrm{I}(t)$ from ECI to ECEF and the associated Direction Cosine Matrix (DCM) $C_{\mathbf{q}_\mathrm{E}^\mathrm{I}}(t)$ are related to their initial values as follows:

$$C_{\mathbf{q}_\mathrm{E}^\mathrm{I}}(t) = \begin{bmatrix} \cos\omega_\mathrm{E} t & \sin\omega_\mathrm{E} t & 0 \\ -\sin\omega_\mathrm{E} t & \cos\omega_\mathrm{E} t & 0 \\ 0 & 0 & 1 \end{bmatrix} C_{\mathbf{q}_\mathrm{E}^\mathrm{I}}(0) \tag{1}$$

Being an orthonormal transformation, the inverse DCM is defined as $C_{\mathbf{q}_\mathrm{I}^\mathrm{E}}(t) = C^{-1}_{\mathbf{q}_\mathrm{E}^\mathrm{I}}(t) = C^{\mathrm{T}}_{\mathbf{q}_\mathrm{E}^\mathrm{I}}(t)$.

For a more intuitive analysis of launch trajectories, see Fig. 1, the Launch Pad (LP) reference frame is fixed at the initial position $\mathbf{r}_\mathrm{I}(0)$ and specified by $\{\mathbf{i}_\mathrm{L}, \mathbf{j}_\mathrm{L}, \mathbf{k}_\mathrm{L}\}$. Here, $\mathbf{k}_\mathrm{L}$ is normal to the local horizon, $\mathbf{i}_\mathrm{L}$ indicates the direction of launch, with an azimuth χ relative to the North, and $\mathbf{j}_\mathrm{L}$ completes a right-handed set. The reference mission addressed in this study (see Sec. III.A) is based on a satellite injection in a quasi-polar orbit, with $\chi \approx -0.02$ degrees. Equivalently, vectors specifying a Recovery Pad (RP) reference frame $\{\mathbf{i}_\mathrm{R}, \mathbf{j}_\mathrm{R}, \mathbf{k}_\mathrm{R}\}$ are defined in the same way, but having the origin at a recovery platform position.

The transformations between ECEF and local frames, $C_{\mathbf{q}_\mathrm{L}^\mathrm{E}}$ and $C_{\mathbf{q}_\mathrm{R}^\mathrm{E}}$, are time-invariant and of straightforward computation [13]. To determine the position and velocity relative to the LP frame, its origin and the contribution of the Earth's rotation must be accounted for as follows:

$$\begin{cases} \mathbf{r}_\mathrm{L}(t) = C_{\mathbf{q}_\mathrm{L}^\mathrm{E}} C_{\mathbf{q}_\mathrm{E}^\mathrm{I}}(t) \left[\mathbf{r}_\mathrm{I}(t) - \mathbf{r}_\mathrm{I}(0)\right] \\ \mathbf{v}_\mathrm{L}(t) = C_{\mathbf{q}_\mathrm{L}^\mathrm{E}} C_{\mathbf{q}_\mathrm{E}^\mathrm{I}}(t) \left[\mathbf{v}_\mathrm{I}(t) - \boldsymbol{\Omega}_\mathrm{I} \times \mathbf{r}_\mathrm{I}(t)\right] \end{cases} \tag{2}$$

with $C_{\mathbf{q}_\mathrm{E}^\mathrm{I}}(t)$ given by Eq. (1), and in the same way for the RP frame. The latter frame is defined based on the location of the recovery platform, which is well-known when the mission starts.

Then, the vehicle's body-fixed reference frame is fixed to its centre of gravity (CG) and has basis vectors $\{\mathbf{i}_\mathrm{B}, \mathbf{j}_\mathrm{B}, \mathbf{k}_\mathrm{B}\}$. Vector $\mathbf{i}_\mathrm{B}$ lies along the vehicle's longitudinal axis and $\mathbf{j}_\mathrm{B}$ is defined so as to remain perpendicular to the pitch plane and have a positive pitch angle. The relationships between LP, RP and body-fixed frames are illustrated in Fig. 1. Note that the pitch plane changes slightly throughout the trajectory as a result of Earth's rotation.

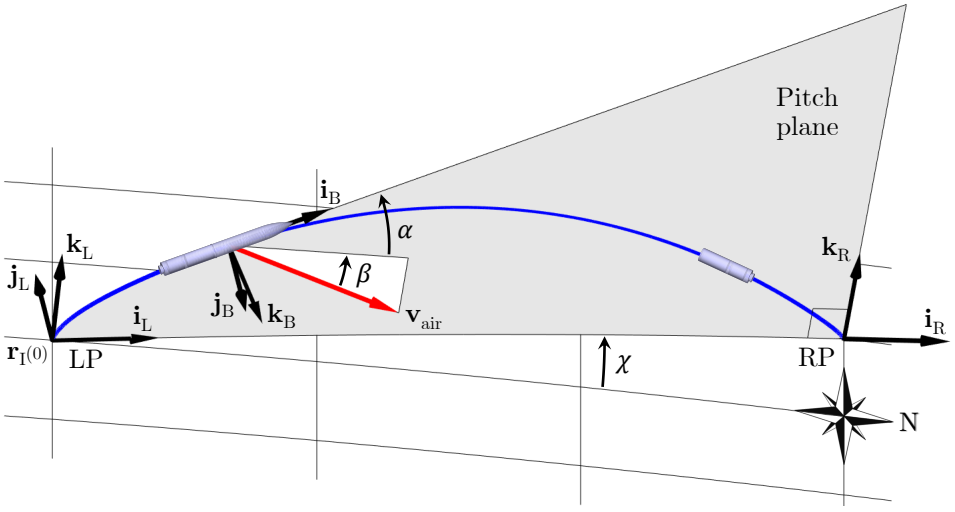

Fig. 1 Relationships between local (launch and recovery pad) and body-fixed reference frames

Following this definition, roll, pitch and yaw angles $\{\phi(t), \theta(t), \psi(t)\}$ represent the orientation of the body-fixed

frame with respect to the LP frame. Hence, upon launch, i.e. $\{\phi(0),\, \theta(0),\, \psi(0)\} = \{\pi,\, \frac{\pi}{2}, 0\}$ radians, the inertial orientation of the vehicle's body is given by:

$$C_{\mathbf{q}_{\mathrm{B}}^{\mathrm{I}}}(0) = \begin{bmatrix} 0 & 0 & 1 \\ 0 & -1 & 0 \\ 1 & 0 & 0 \end{bmatrix} C_{\mathbf{q}_{\mathrm{L}}^{\mathrm{E}}}\, C_{\mathbf{q}_{\mathrm{E}}^{\mathrm{I}}}(0) \tag{3}$$

and its initial angular velocity corresponds to $\omega_{\mathrm{B}}(0) = C_{\mathbf{q}_{\mathrm{B}}^{\mathrm{I}}}(0)\, \mathbf{\Omega}_{\mathrm{I}}$. The offset between launch pad and the vehicle's CG can be neglected for practical computations.

For the computation of the aerodynamic characteristics, a velocity reference frame (VRF) is defined using vectors $\{\mathbf{i}_{\mathrm{V}},\, \mathbf{j}_{\mathrm{V}},\, \mathbf{k}_{\mathrm{V}}\}$. This frame is also fixed to the vehicle's CG, but now with $\mathbf{i}_{\mathrm{V}}$ directed along the air-relative velocity vector $\mathbf{v}_{\mathrm{air}}(t)$. A vector rotation from the body-fixed to VRF, $C_{\mathbf{q}_{\mathrm{V}}^{\mathrm{B}}}(t)$, can be represented by two aerodynamic angles, the angle of attack $\alpha(t)$ and sideslip $\beta(t)$ (also depicted in Fig. 1), as follows:

$$C_{\mathbf{q}_{\mathrm{V}}^{\mathrm{B}}}(t) = \begin{bmatrix} \cos\alpha(t)\, \cos\beta(t) & \sin\beta(t) & \sin\alpha(t)\, \cos\beta(t) \\ -\cos\alpha(t)\, \sin\beta(t) & \cos\beta(t) & -\sin\alpha(t)\, \sin\beta(t) \\ -\sin\alpha(t) & 0 & \cos\alpha(t) \end{bmatrix} \tag{4}$$

The gravity model adopted in this study is the 2008 Earth Gravitational Model [14] (EGM), which is based on a 120th order spherical harmonic approximation of the gravity field and implemented in [13]. It contains a function $\mathbf{g}_{\mathrm{EGM}}$ that computes the gravity acceleration in the ECEF frame. Hence, the corresponding vector in inertial coordinates is given by:

$$\mathbf{g}_{\mathrm{I}}(t) = C_{\mathbf{q}_{\mathrm{I}}^{\mathrm{E}}}(t)\, \mathbf{g}_{\mathrm{EGM}}\left(C_{\mathbf{q}_{\mathrm{E}}^{\mathrm{I}}}(t)\, \mathbf{r}_{\mathrm{I}}(t)\right) \tag{5}$$

The atmosphere model adopted is also available in [13] and implements the mathematical representation of the 1976 Committee on Extension to the Standard Atmosphere [15] (COESA). This representation provides, as a function of altitude, the air density $\rho\,(h(t))$ and the speed of sound $a\,(h(t))$.

Finally, wind gusts are included by adding an altitude-dependent velocity field with Northern and Eastern components, $w_{\mathrm{NRN}}\,(h(t))$ and $w_{\mathrm{ERN}}\,(h(t))$ relative to launch pad, hence the wind perturbation with respect to the ECEF frame corresponds to:

$$\mathbf{w}_{\mathrm{E}}(t) = C_{\mathbf{q}_{\mathrm{E}}^{\mathrm{L}}} \begin{bmatrix} \cos\chi & \sin\chi \\ \sin\chi & -\cos\chi \\ 0 & 0 \end{bmatrix} \begin{bmatrix} w_{\mathrm{NRN}}\,(h(t)) \\ w_{\mathrm{ERN}}\,(h(t)) \end{bmatrix} \tag{6}$$

$w_{\mathrm{NRN}}\,(h(t))$ and $w_{\mathrm{ERN}}\,(h(t))$ can be generated, for example, using traditional noise-colouring Dryden filters.

B. Equations of Motion

The dynamic equations that describe the motion of a vehicle in space are summarised below and complete derivations can be found in [10] and [16]. These equations are based on the initial states $\{\mathbf{r}_{\mathrm{I}}(0),\ \mathbf{v}_{\mathrm{I}}(0),\ \mathbf{q}_{\mathrm{B}}^{\mathrm{I}}(0),\ \omega_{\mathrm{B}}(0)\}$ identified in Sec. II.A and on the assumption that effects related to MCI time-derivatives ($\dot{m}$ and $\dot{J}$) and moving masses (including "tail-wags-dog" moment and rocket jet damping) are negligible for trajectory assessment.

The vehicle's translational motion (i.e. acceleration $\ddot{\mathbf{r}}_{\mathrm{I}}(t)$ and velocity $\mathbf{v}_{\mathrm{I}}(t)$) is described in the ECI frame by:

$$\ddot{\mathbf{r}}_{\mathrm{I}}(t) = \dot{\mathbf{v}}_{\mathrm{I}}(t) = \mathbf{g}_{\mathrm{I}}(t) + \frac{1}{m(t)}\left[\mathbf{F}_{\mathrm{aero,I}}(t) + \mathbf{F}_{\mathrm{TVC,I}}(t) + \mathbf{F}_{\mathrm{fins,I}}(t) + \mathbf{F}_{\mathrm{thr,I}}(t)\right] \tag{7}$$

where $\mathbf{F}_{\mathrm{aero,I}}(t)$ represents the aerodynamic force of the vehicle's body (Sec. II.C) expressed in the ECI frame, $\mathbf{F}_{\mathrm{TVC,I}}(t)$, $\mathbf{F}_{\mathrm{fins,I}}(t)$ and $\mathbf{F}_{\mathrm{thr,I}}(t)$ represent control forces (Sec. II.D to II.F), $m(t)$ is the total mass of the vehicle (Sec. II.G) and $\mathbf{g}_{\mathrm{I}}(t)$ is given by Eq. (5).

In addition, the rotational dynamics (i.e. angular velocity $\omega_{\mathrm{B}}(t)$) is described in the body-fixed frame by:

$$\dot{\omega}_{\mathrm{B}}(t) = J^{-1}(t)\left[\mathbf{M}_{\mathrm{aero,B}}(t) + \mathbf{M}_{\mathrm{TVC,B}}(t) + \mathbf{M}_{\mathrm{fins,B}}(t) + \mathbf{M}_{\mathrm{thr,B}}(t) - \omega_{\mathrm{B}}(t) \times J(t)\,\omega_{\mathrm{B}}(t)\right] \tag{8}$$

Equivalently to the forces, $\mathbf{M}_{\mathrm{aero,B}}(t)$, $\mathbf{M}_{\mathrm{TVC,B}}(t)$, $\mathbf{M}_{\mathrm{fins,B}}(t)$ and $\mathbf{M}_{\mathrm{thr,B}}(t)$ represent aerodynamic and control moments written in the body axes, and $J(t)$ is the inertia tensor of the vehicle (Sec. II.G).

Finally, the orientation of the vehicle's body axes in the ECI frame is propagated by the kinematics:

$$\dot{\mathbf{q}}_{\mathrm{B}}^{\mathrm{I}}(t) = \frac{1}{2}\begin{bmatrix} q_4(t) & -q_3(t) & q_2(t) \\ q_3(t) & q_4(t) & -q_1(t) \\ -q_2(t) & q_1(t) & q_4(t) \\ -q_1(t) & -q_2(t) & -q_3(t) \end{bmatrix}\omega_{\mathrm{B}}(t) \tag{9}$$

where quaternion $\mathbf{q}_{\mathrm{B}}^{\mathrm{I}}(t) = [q_1(t);\ q_2(t);\ q_3(t);\ q_4(t)]$ is assumed to have the scalar component as its last position, i.e. $q_4(t)$. This vector and its associated DCM $C_{\mathbf{q}_{\mathrm{B}}^{\mathrm{I}}}(t)$ are also essential for the computation of the forces and moments in Eq. (7) and (8).

The equations of motion can be easily augmented to include effects such as structural flexibility and propellant sloshing. However, in this study, only rigid-body motion is considered.

C. Aerodynamics Characteristics

Aerodynamic forces and moments generated by the vehicle's main body depend on its external shape, as well on the instantaneous dynamic pressure. Assuming that the Earth's atmosphere rotates with the planet without slippage and shearing, dynamic pressure is given by:

$$Q(t) = \frac{1}{2}\rho(t)\,\|\mathbf{v}_{\text{air}}(t)\|^2 \tag{10}$$

where $\mathbf{v}_{\text{air}}(t) = [v_{\text{air,x}}(t);\ v_{\text{air,y}}(t);\ v_{\text{air,z}}(t)]$ is the air-relative velocity vector written in the body-fixed frame. This vector accounts for the vehicle's inertial velocity $\mathbf{v}_{\text{I}}(t)$, Earth's rotation $\boldsymbol{\Omega}_{\text{I}}$ and wind gusts $\mathbf{w}_{\text{E}}(t)$ as follows:

$$\mathbf{v}_{\text{air}}(t) = C_{\mathbf{q}_{\text{B}}^{\text{I}}}(t)\,[\mathbf{v}_{\text{I}}(t) - \boldsymbol{\Omega}_{\text{I}} \times \mathbf{r}_{\text{I}}(t) - C_{\mathbf{q}_{\text{I}}^{\text{E}}}(t)\,\mathbf{w}_{\text{E}}(t)] \tag{11}$$

and allows to define the aerodynamic angles:

$$\begin{cases} \alpha(t) = \arctan_2 \dfrac{v_{\text{air,z}}(t)}{v_{\text{air,x}}(t)} \\ \beta(t) = \arcsin \dfrac{v_{\text{air,y}}(t)}{\|\mathbf{v}_{\text{air}}(t)\|} \end{cases} \tag{12}$$

The vehicle has a generic axis-symmetric shape that is representative of Europe's lightweight VEGA launcher [17]. Having in mind its axisymmetry, the forces are expressed in the air-relative velocity reference frame as:

$$\mathbf{F}_{\text{aero,V}}(t) = -Q(t)S_{\text{ref}} \begin{bmatrix} C_D\left(\alpha_{\text{eff}}(t), M(t)\right) \\ 0 \\ C_L\left(\alpha_{\text{eff}}(t), M(t)\right) \end{bmatrix} \tag{13}$$

where S_{ref} is a reference aerodynamic area and $\{C_D,\ C_L\}$ are the drag and lift coefficients, respectively. These coefficients are estimated as functions of the effective angle of attack $\alpha_{\text{eff}}(t)$ and Mach number $M(t) = \|\mathbf{v}_{\text{air}}(t)\|/a(t)$. The former is defined based on a total angle of attack assumption as follows:

$$\alpha_{\text{eff}}(t) = \arccos\left(\cos\alpha(t)\,\cos\beta(t)\right) \approx \sqrt{\alpha^2(t) + \beta^2(t)} \tag{14}$$

The aerodynamic force of Eq. (13) is thus written in the ECI frame as:

$$\mathbf{F}_{\text{aero,I}}(t) = C_{\mathbf{q}_{\text{I}}^{\text{B}}}(t)\,C_{\mathbf{q}_{\text{B}}^{\text{V}}}(t)\,\mathbf{F}_{\text{aero,V}}(t) \tag{15}$$

In addition, for the equations of motion, it is assumed that the aerodynamic moment generated around the vehicle's

CG is only caused by the offset between this point and the centre of pressure (CP), where aerodynamic forces are applied. Hence, the aerodynamic moment is directly expressed in the body-fixed frame as:

$$\mathbf{M}_{\text{aero,B}}(t) = [\mathbf{x}_{\text{CP}}(t) - \mathbf{x}_{\text{CG}}(t)] \times C_{\mathbf{q}_{\text{B}}^{\text{V}}}(t)\, \mathbf{F}_{\text{aero,V}}(t) \tag{16}$$

In this equation, the vectors $\mathbf{x}_{\text{CP}}(t) = [x_{\text{CP}}(t);\, 0;\, 0]$ and $\mathbf{x}_{\text{CG}}(t) = [x_{\text{CG}}(t);\, y_{\text{CG}}(t);\, z_{\text{CG}}(t)]$ represent respectively the CP and CG positions with respect to the same reference point in the body-fixed frame. Similar to the drag and lift coefficients, x_{CP} is estimated as a function of $\alpha_{\text{eff}}(t)$ and $M(t)$, while the evolution of $\mathbf{x}_{\text{CG}}(t)$ is computed in Sec. II.G.

Aerodynamic coefficients were kindly provided by AVIO using the full vehicle configuration up to a 10 degree angle of attack and for the post-separation configuration sparsely from 0 to 180 degrees angles of attack. These coefficients are then linearly interpolated. x_{CP} is not defined for $\alpha_{\text{eff}}(t)$ equal to 0 and 180 degrees, hence it is linearly extrapolated from the adjacent interval. The variation of C_D, C_L and x_{CP} for these two cases with respect to α_{eff} and M is illustrated in Fig. 2 and 3 respectively.

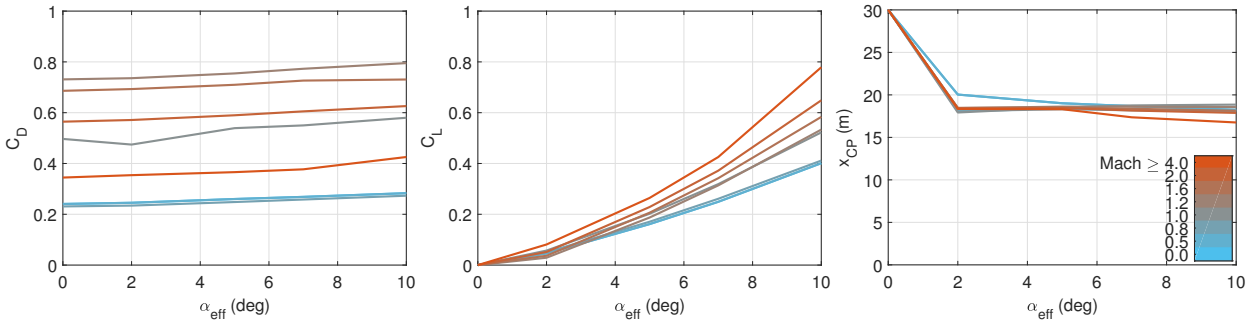

(a) C_D (b) C_L (c) x_{CP} relative to body base

Fig. 2 Aerodynamic coefficients for full vehicle configuration

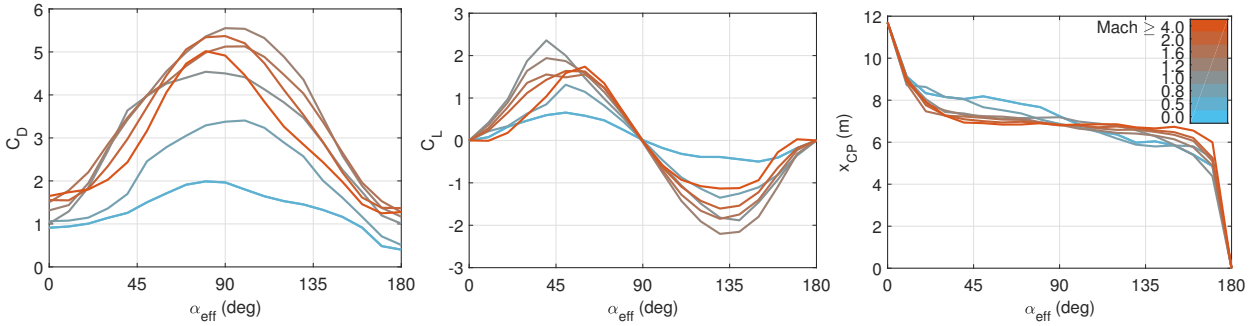

(a) C_D (b) C_L (c) x_{CP} relative to body base

Fig. 3 Aerodynamic coefficients for first stage configuration

For simplicity, aerodynamic coefficients are assumed to be independent of the level of thrust, which is a very rough approximation for retro-propulsive flight, where there are complicated interactions between the engine plume and the oncoming flow [18]. In addition, the sparsity of the available data results in limited fidelity around certain conditions (e.g. $M \rightarrow 1$ and $\alpha_{\text{eff}} \rightarrow 0$), hence the generalised use of the provided coefficients must be subject to caution. Nonetheless, the above limitations do not invalidate the modelling approach and the adopted model can be easily upgraded.

In addition, the proneness of the vehicle to generate aerodynamic loads is conventionally quantified using the parameter:

$$\mu_\alpha(t) = [x_{\text{CP}}(t) - x_{\text{CG}}(t)] \, \frac{S_{\text{ref}} \, C_{N_\alpha}(t)}{J_N(t)} \, Q(t) \tag{17}$$

In other words, this parameter provides an affine relationship between the angle of attack and the load-induced angular acceleration [10] as follows:

$$[x_{\text{CP}}(t) - x_{\text{CG}}(t)] \, \frac{S_{\text{ref}} \, C_{N_\alpha}(t)}{J_N(t)} \, Q(t) \, \alpha_{\text{eff}}(t) = \mu_\alpha(t) \, \alpha_{\text{eff}}(t) \tag{18}$$

Here, $J_N(t)$ is the lateral moment of inertia (MoI) component and $C_{N_\alpha}(t) = \partial C_N \left(\alpha(t), M(t)\right) / \partial \alpha(t)$ is the normal load gradient, with:

$$C_N \left(\alpha(t), M(t)\right) = C_L \left(\alpha(t), M(t)\right) \cos \alpha(t) + C_D \left(\alpha(t), M(t)\right) \sin \alpha(t) \tag{19}$$

In Eq. (18), all the terms except for $Q_\alpha(t) := Q(t) \, \alpha_{\text{eff}}(t)$ are mostly vehicle-depend. Hence, $Q_\alpha(t)$ is an extremely useful indicator as it directly assesses the impact of trajectory and attitude on the induced loads. For physically meaningful results, $\alpha_{\text{eff}}(t)$ must always be reduced to the first quadrant.

Finally, it is also essential to have an idea of the thermal environment encountered by the RLV throughout L&R. A simple way to achieve this is by analysing the heat flux at the vehicle's stagnation point [11]. Given a reference nose radius R_{ref}, the maximum heat rate can be approximated by the Sutton Graves equation:

$$Q_H(t) = k_H \sqrt{\frac{\rho(t)}{R_{\text{ref}}}} \, \|\mathbf{v}_{\text{air}}(t)\|^3 \tag{20}$$

with $k_H \approx 1.74 \times 10^{-4}$ for Earth and $R_{\text{ref}} = 1.5$ m.

D. Thrust Vector Control

The vehicle's ascent and descent trajectories are controlled by adjusting the magnitude and direction of the thrust vector generated by its rocket engine. This adjustment is achieved via two TVC actuators that deflect the engine's nozzle by $\{\beta_{\text{TVC,y}}(t), \, \beta_{\text{TVC,z}}(t)\}$ along the body $\mathbf{j}_{\text{B}}$ and $\mathbf{k}_{\text{B}}$ axes respectively.

The required thrust magnitude $T_{\text{ref}}(t)$ and direction are commanded by the guidance subsystem (Sec. III), with

the latter using vehicle attitude reference angles $\{\phi_{\text{ref}}(t),\, \theta_{\text{ref}}(t),\, \psi_{\text{ref}}(t)\}$ as a surrogate. This decoupling between translational and rotational dynamics is common practice and often a good approximation since the vehicle's attitude can be changed considerably faster than its trajectory.

With this in mind, the TVC-generated force becomes:

$$\mathbf{F}_{\text{TVC,B}}(t) = T_{\text{ref}}(t) \begin{bmatrix} \cos\beta_{\text{TVC,y}}(t)\, \cos\beta_{\text{TVC,z}}(t) \\ \cos\beta_{\text{TVC,y}}(t)\, \sin\beta_{\text{TVC,z}}(t) \\ -\sin\beta_{\text{TVC,y}}(t) \end{bmatrix} \tag{21}$$

$$\mathbf{F}_{\text{TVC,I}}(t) = C_{\mathbf{q}_{\text{I}}^{\text{B}}}(t)\, \mathbf{F}_{\text{TVC,B}}(t) \tag{22}$$

and, with $\mathbf{x}_{\text{PVP}} = [x_{\text{PVP}};\, 0;\, 0]$ representing the TVC pivot position, the moment around the CG is given by:

$$\mathbf{M}_{\text{TVC,B}}(t) = [\mathbf{x}_{\text{PVP}} - \mathbf{x}_{\text{CG}}(t)] \times \mathbf{F}_{\text{TVC,B}}(t) \tag{23}$$

Similar to Eq. (17), the TVC effectiveness in counteracting aerodynamic loads is measured through the coefficient:

$$\mu_{\text{c}}(t) = [x_{\text{CG}}(t) - x_{\text{PVP}}]\, \frac{T_{\text{ref}}(t)}{J_N(t)} \tag{24}$$

which is naturally driven by $T_{\text{ref}}(t)$. This coefficient establishes an affine approximation between in-plane TVC deflection and control-induced angular acceleration:

$$[x_{\text{CG}}(t) - x_{\text{PVP}}]\, \frac{T_{\text{ref}}(t)}{J_N(t)}\, \sin\beta_{\text{TVC,z}}(t) \approx \mu_{\text{c}}(t)\, \beta_{\text{TVC,z}}(t) \tag{25}$$

The generation of thrust then causes the depletion of propellant. In this case, assuming negligible engine back-pressure losses, the mass-depletion dynamics is given by the rocket equation [10]:

$$\dot{m}(t) = -\frac{1}{I_{\text{sp}} g_0}\, T_{\text{ref}}(t) \tag{26}$$

where I_{sp} is the specific impulse of the engine, which is assumed constant for simplicity, and $g_0 \approx 9.81$ m/s^2 is the gravitational acceleration at the Earth's surface.

Recovering the launch vehicle requires the use of a re-ignitable and throttleable rocket engine. For this study, a fictional liquid engine using highly-refined kerosene (RP-1) as fuel and liquid oxygen (LOx) as oxidizer is adopted. This type of engine is common among many launcher manufacturers [12], including SpaceX [19]. Its main characteristics are summarised in Table 1.

Table 1 RLV Rocket engine characteristics

Parameter	Value
Specific impulse (s)	282
Oxidizer/fuel mass ratio	2.56
Oxidizer/fuel density ratio	1.42
Initial fuel mass (kg)	25913
Initial oxidizer mass (kg)	66337

In this table, the required initial propellant masses have been determined based on the reference mission under analysis and on information from the VEGA launcher [17]. In order for the tanks to meet VEGA's dimensions and initial MCI properties while ensuring that the remaining propellant after launch is enough for a powered descent, this results in a structural mass lower than the original one and in propellant densities higher than the actual LOx/RP engine. Nevertheless, the same density ratio of Table 1 is kept so as to have a meaningful representation of the CG travel throughout the burn. Further details on the launcher's MCI evolution are provided in Sec. II.G.

E. Fins

Fin actuators are also included in the RLV model to ensure enough control authority under low (or zero) TVC effectiveness (recall Eq. (24)). This will be particularly critical throughout the descent flight, and thus they should be ideally placed above the vehicle's centre of pressure during this phase for improved stability. Here, only two pairs of fins are considered as depicted in Fig. 4, but the generalisation in case additional surfaces are exploited for improved controllability is straightforward.

One pair of fins is then assigned to pitch motion control using deflections $\{\beta_{\text{fin},1}(t),\ \beta_{\text{fin},2}(t)\}$, the other pair to yaw control via $\{\beta_{\text{fin},3}(t),\ \beta_{\text{fin},4}(t)\}$ and it is assumed that any roll perturbation is rejected by the attitude control system (see Sec. IV) so that the two pairs always remain in the trajectory yaw and pitch planes, respectively.

It is further assumed that, due to the reduced fin area compared to the RLV body, their axial force contribution is negligible so that only the normal component is accounted for. When flow separation is neglected, this contribution has a sinusoidal dependence on the fin angle of attack given by:

$$C_{\text{fin}}\left(\alpha_{\text{fin}}(t)\right) = \bar{C}_{\text{fin}}\ \sin\alpha_{\text{fin}}(t) \tag{27}$$

where $\bar{C}_{\text{fin}}$ is the maximum normal fin force coefficient and $\alpha_{\text{fin}}(t)$ is the local angle of attack. The impact of these assumptions will be verified at a later stage through the consideration of aerodynamic uncertainties in the model.

The i^{th} fin's angle of attack and its associated force in the RLV body-fixed frame $\mathbf{F}_{\text{fin},i}(t)$ are then defined in the pitch plane as:

$$\begin{cases} \alpha_{\text{fin},i}(t) = \beta_{\text{fin},i}(t) - \alpha(t), & i = \{1,2\} \\ \mathbf{F}_{\text{fin},i}(t) = Q(t) S_{\text{fin}} C_{\text{fin}} \left(\alpha_{\text{fin},i}(t)\right) \left[-\sin\beta_{\text{fin},i}(t) \quad 0 \quad \cos\beta_{\text{fin},i}(t)\right]^{\text{T}}, & i = \{1,2\} \end{cases} \tag{28}$$

and in the yaw plane as:

$$\begin{cases} \alpha_{\text{fin},i}(t) = -\beta_{\text{fin},i}(t) - \beta(t), & i = \{3,4\} \\ \mathbf{F}_{\text{fin},i}(t) = Q(t) S_{\text{fin}} C_{\text{fin}} \left(\alpha_{\text{fin},i}(t)\right) \left[\sin\beta_{\text{fin},i}(t) \quad \cos\beta_{\text{fin},i}(t) \quad 0\right]^{\text{T}}, & i = \{3,4\} \end{cases} \tag{29}$$

where S_{fin} is the surface area of one fin and $\alpha(t)$, $\beta(t)$ and $Q(t)$ are from Sec. II.C. With this in mind, the fin-generated force in the ECI frame and the moment in the body frame correspond to:

$$\mathbf{F}_{\text{fins,I}}(t) = C_{\mathbf{q}_{\text{I}}^{\text{B}}}(t) \sum_{i=1}^{4} \mathbf{F}_{\text{fin},i}(t) \tag{30}$$

$$\mathbf{M}_{\text{fins,B}}(t) = \sum_{i=1}^{4} \left[\mathbf{x}_{\text{fin},i} - \mathbf{x}_{\text{CG}}(t)\right] \times \mathbf{F}_{\text{fin},i}(t) \tag{31}$$

where the offset between each fin's CP and attachment point $\mathbf{x}_{\text{fin},i}$ is negligible compared to the distance between the latter and the vehicle's CG, see Fig. 4.

Once again, the effectiveness of the fins in generating control moments can be quantified. Assuming equal fin deflections within the same plane, it is given by:

$$\mu_{\text{f}}(t) = 2\,\left[x_{\text{fin}} - x_{\text{CG}}(t)\right]\,\frac{Q(t)\,S_{\text{fin}}\,C_{\text{fin}_\alpha}(t)}{J_N(t)} \tag{32}$$

where x_{fin} is the longitudinal position of the fins and $C_{\text{fin}_\alpha}(t) = \bar{C}_{\text{fin}}\,\cos\alpha_{\text{fin}}(t)$ is the normal fin force gradient, with $\alpha_{\text{fin}}(t)$ computed from Eq. (28) for the pitch plane (or from Eq. (29) for the yaw plane).

Because $\alpha_{\text{fin}}(t)$ has a dependence on $\alpha(t)$ (or $\beta(t)$), the fins will also have an impact on the natural aerodynamics of the vehicle and its load-proneness parameter is generalised accordingly:

$$\mu_{\alpha'}(t) = \mu_{\alpha}(t) + \mu_{\text{f}}(t) \tag{33}$$

For the rest of this study, $\bar{C}_{\text{fin}}$ has been fixed to 6, which is a reasonable value among conventional symmetrical airfoils, and S_{fin} has been set to 0.54 m^2 based on preliminary stability analyses (see Sec. IV.A).

F. Cold Gas Thrusters

In addition, cold gas thrusters are included for controllability under zero main engine thrust and low fin effectiveness (recall Eq. (32)), which is the case at high altitudes where air density is very low.

Similar to the fins, a different pair of thrusters is assigned to pitch and yaw control. The force generated in the ECI frame is given by:

$$\mathbf{F}_{\text{thr,I}}(t) = C_{\mathbf{q}_{\text{I}}^{\text{B}}}(t)\,\bar{T}_{\text{thr}}\left(\beta_{\text{thr,y}}(t)\,\mathbf{k}_{\text{B}} - \beta_{\text{thr,z}}(t)\,\mathbf{j}_{\text{B}}\right) \tag{34}$$

where $\bar{T}_{\text{thr}}$ is the maximum thruster force and $\{\beta_{\text{thr,y}}(t),\ \beta_{\text{thr,z}}(t)\}$ are attitude commands about the body $\mathbf{j}_{\text{B}}$ and $\mathbf{k}_{\text{B}}$ axes, normalised between $[-1,\ 1]$. Equivalently, the corresponding moment in the body-fixed frame is:

$$\mathbf{M}_{\text{thr,B}}(t) = \bar{T}_{\text{thr}}\left(\left[\mathbf{x}_{\text{thr,y}} - \mathbf{x}_{\text{CG}}(t)\right] \times \beta_{\text{thr,y}}(t)\,\mathbf{k}_{\text{B}} - \left[\mathbf{x}_{\text{thr,z}} - \mathbf{x}_{\text{CG}}(t)\right] \times \beta_{\text{thr,z}}(t)\,\mathbf{j}_{\text{B}}\right) \tag{35}$$

In this equation, $\mathbf{x}_{\text{thr,y}}$ and $\mathbf{x}_{\text{thr,z}}$ represent the position of the thruster that is triggered for pitch and yaw control, which has to be adjusted in accordance with the sign of $\beta_{\text{thr,y}}(t)$ and $\beta_{\text{thr,z}}(t)$ since commands in opposite directions trigger thrusters in opposite sides of the vehicle. For simplicity, thruster commands are assumed to be continuous in this study.

Once again, control effectiveness of cold gas thrusters can also be quantified as follows:

$$\mu_{\text{t}}(t) = \left[x_{\text{thr}} - x_{\text{CG}}(t)\right]\,\frac{\bar{T}_{\text{thr}}}{J_N(t)} \tag{36}$$

where x_{thr} is the longitudinal position of the thrusters (here assumed equal to x_{fin} for simplicity). In addition, $\bar{T}_{\text{thr}}$ is fixed to 400 N, which is a reasonable value among conventional actuators.

It is also important to note that, although there is a mass budget and depletion associated to cold gas thrusters, it is assumed to be negligible compared to that of the main engine.

G. Mass, CG & Inertia Evolution

In line with all the considerations above, the launcher configuration adopted is detailed in Fig. 4, showing the full vehicle on the left and the reusable first stage on the right. Since this study is focused on the ascent and descent flight of the first stage only, all the other vehicle bodies (e.g. upper stages) will be referred to as payload (PL) from the perspective of the first stage.

The vehicle is assumed to have an axis-symmetric shape and a uniform material (dry) density, with more mass allocated to the bottom and middle sections to account for the weight of the main engine module, retractable landing gear and inter-tank adapter. Moreover, fuel and oxidizer masses are modelled as cylinders in end-burn, see [16].

The MCI properties of the dry first stage and payload are summarised in Table 2. In this table, and for the remainder of this section, heights are measured with respect to the first stage body base (i.e. 0.66 m above the nozzle exit), and

moments of inertia (MoI) are relative to the CG of the corresponding body.

Based on this configuration, the vehicle's mass, which is updated via Eq. (26) during engine burn, breaks down into:

$$m(t) = m_{\text{prop}}(t) + m_{\text{dry}} + m_{\text{PL}} \tag{37}$$

with m_{dry} and m_{PL} given in Table 2 and propellant mass defined as $m_{\text{prop}}(t) = m_{\text{fuel}}(t) + m_{\text{oxid}}(t)$. Note that m_{PL} must be set to 0 after separation.

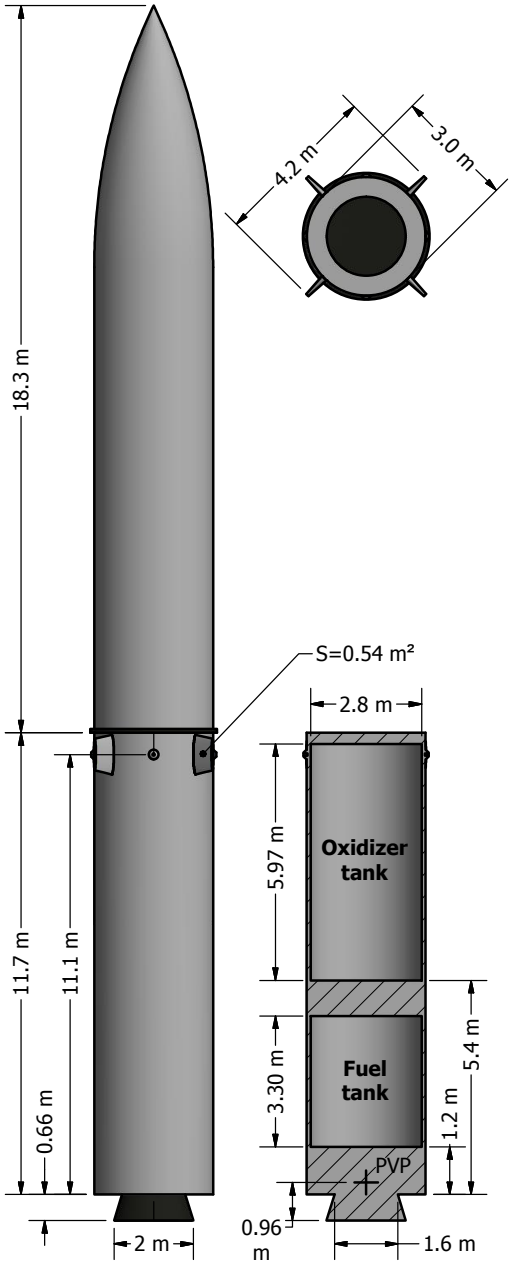

Fig. 4 Generic RLV and first stage configuration

Table 2 RLV Structural characteristics

	Dry first stage	Payload total
Mass (kg)	2750	43000
CG Height (m)	4.60	12.91
MoI Axial (kg m^2)	3981	44000
MoI Lateral (kg m^2)	40267	3×10^6

In order to compute the change over time of fuel and oxidizer masses, $m_{\text{fuel}}(t)$ and $m_{\text{oxid}}(t)$, as well as their level on the corresponding tank, $h_{\text{fuel}}(t)$ and $h_{\text{oxid}}(t)$, it is useful to normalise the propellant mass with respect to the initial values of Table 1:

$$\eta(t) = \frac{m_{\text{prop}}(t)}{m_{\text{prop}}(0)} \tag{38}$$

$$m_{\#}(t) = \eta(t)\, m_{\#}(0) \tag{39}$$

$$h_{\#}(t) = \eta(t)\, d_{\text{tk},\#} \tag{40}$$

where # = {fuel, oxid} and $d_{\text{tk,fuel}}$ and $d_{\text{tk,oxid}}$ are the tank depths depicted in Fig. 4 (3.30 and 5.97 m, respectively). The ratio between propellant burnt and its initial value can also be directly quantified as:

$$\frac{m_{\text{burnt}}(t)}{m_{\text{prop}}(0)} = 1 - \eta(t) \tag{41}$$

Due to propellant mass and level variations, the total vehicle CG and MoI vary substantially throughout the flight. In the nominal case, the former lies along the body longitudinal axis, $\mathbf{x}_{\text{CG}}(t) = [x_{\text{CG}}(t);\, 0;\, 0]$, and is computed as:

$$x_{\text{CG}}(t) = \frac{1}{m(t)} \left[m_{\text{fuel}}(t) \left(h_{\text{tk,fuel}} + \frac{h_{\text{fuel}}(t)}{2} \right) + m_{\text{oxid}}(t) \left(h_{\text{tk,oxid}} + \frac{h_{\text{oxid}}(t)}{2} \right) + m_{\text{dry}}\, h_{\text{dry}} + m_{\text{PL}}\, h_{\text{PL}} \right] \tag{42}$$

where $h_{\text{tk,fuel}}$ (1.2 m) and $h_{\text{tk,oxid}}$ (5.4 m) are the tank heights provided in Fig. 4 and h_{dry} and h_{PL} are given in Table 2.

Based on the same assumptions, the inertia tensor is diagonal in nominal conditions and can be expressed as $J(t) = \text{diag}\,[J_A(t);\, J_N(t);\, J_N(t)]$. The axial component corresponds directly to:

$$J_A(t) = \frac{1}{2}\, m_{\text{prop}}(t)\, r_{\text{tk}}^2 + J_{A,\text{dry}} + J_{A,\text{PL}} \tag{43}$$

in which r_{tk} (1.4 m) is the tank radius. The lateral contributions of propellant masses relative to their CG are given by:

$$J_{N,\text{fuel}}(t) = \frac{1}{12} m_{\text{fuel}}(t) \left(3r_{\text{tk}}^2 + h_{\text{fuel}}^2(t)\right) \tag{44}$$

$$J_{N,\text{oxid}}(t) = \frac{1}{12} m_{\text{oxid}}(t) \left(3r_{\text{tk}}^2 + h_{\text{oxid}}^2(t)\right) \tag{45}$$

and all the contributions are converted to vehicle's CG coordinates using the parallel axis theorem as follows:

$$\begin{aligned} J_N(t) = J_{N,\text{fuel}}(t) + J_{N,\text{oxid}}(t) + J_{N,\text{dry}} + J_{N,\text{PL}} + m_{\text{fuel}}(t) \left(h_{\text{tk,fuel}} + \frac{h_{\text{fuel}}(t)}{2} - x_{\text{CG}}(t)\right)^2 + \\ + m_{\text{oxid}}(t) \left(h_{\text{tk,oxid}} + \frac{h_{\text{oxid}}(t)}{2} - x_{\text{CG}}(t)\right)^2 + m_{\text{dry}} \left(h_{\text{dry}} - x_{\text{CG}}(t)\right)^2 + m_{\text{PL}} \left(h_{\text{PL}} - x_{\text{CG}}(t)\right)^2 \end{aligned} \tag{46}$$

Once again, m_{PL}, $J_{A,\text{PL}}$ and $J_{N,\text{PL}}$ are set to 0 after separation and $x_{\text{CG}}(t)$ is computed via Eq. (42).

III. RLV Guidance Approach

This section provides a description of the guidance techniques considered in this study for the coupled assessment of RLVs. First, a general introduction of the reference mission profile and booster-back recovery strategies is presented, followed by the presentation of the baseline landing algorithm currently implemented.

A. Launch & Recovery Mission Profiles

In recent years, several studies [2–6] have addressed the problem of RLV performance optimisation. These are mostly focused on the application of multi-disciplinary optimisation (MDO) methods to determine L&R trajectories that allow delivering the highest payload while fulfilling competing mission and aerothermal load requirements. In opposition, the present study is not focused on the optimisation of payload capabilities, but rather on analysing the practical feasibility of different descent trajectories, together with the impact of different G&C choices on the aerothermal loads encountered during the flight and on recovery performance.

For the above reason, the launch mission profile and the vehicle configuration described here remain fixed throughout this study and only the recovery trajectory is modified. The ascent profile corresponds to that of a 1,100 kg satellite injection in a quasi-polar orbit at an altitude of 800 km using an expendable launcher from the European Space Centre in French Guiana. Concerning its recovery, two distinct strategies are addressed and discussed below: downrange landing (DRL) and return to launch site (RTLS), see Fig. 5.

The most straightforward booster-back recovery strategy is known as downrange landing (DRL). In this scenario, the idea is for the reusable stage to be landed close to its un-propelled impact site, therefore minimising the propellant required for the landing. However, launches typically take place in the direction of the sea due to safety reasons, thus a sea-going recovery platform needs to be placed at the landing point and then bring the stage back. This approach has

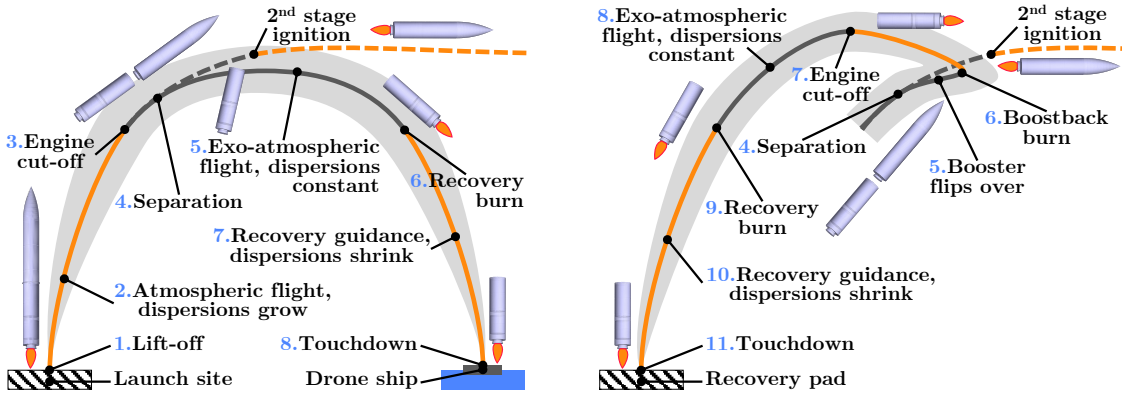

(a) Downrange landing (DRL)

(b) Return to launch site (RTLS)

Fig. 5 Recovery mission profiles

been successfully employed by SpaceX [1], which uses a 91 m by 52 m drone ship as recovery pad.

From Fig. 5a, DRL missions start naturally with lift-off and ascent of the first stage (points 1 and 2 in the figure). This part of the mission is typically flown with open-loop guidance, hence dispersions due to system uncertainties and environmental perturbations tend to grow. These dispersions are then compensated for by the exo-atmospheric stages in order to ensure an accurate satellite injection. Open-loop guidance commands are provided in terms of reference attitude angles $\{\theta_{\text{ref}}(t),\, \psi_{\text{ref}}(t)\}$ relative to the LP frame and thrust magnitude $T_{\text{ref}}(t)$.

The reference profiles adopted in this study are depicted in Fig. 6, where the distinct launch phases of pitch over and gravity turn have been highlighted. The thrust profile (bottom plot) is representative of a (non-throttleable) solid rocket engine and could be optimised for the present liquid-propellant launcher, with important consequences on the staging altitude and Mach number. Nonetheless, as mentioned above, the launch trajectory was kept the same for simplicity. Similar to the simplifications made in the aerodynamics model, it does not invalidate G&C design/analysis for the recovery phase and opens the door to more detailed analyses, featuring a more realistic ascent thrust profile.

After 110 seconds of flight, the first stage cuts off its engine and separates two seconds after (points 3 and 4 of Fig. 5a). The second stage then ignites its engine and proceeds the flight towards the payload's destination orbit. In the meantime (point 5), the first stage continues its exo-atmospheric motion in the direction of the recovery platform with approximately constant dispersions but with increasing velocity due to the action of gravity.

Then, at a pre-specified altitude h_s, the first stage re-ignites its engine for the recovery burn (point 6), which must be able to counteract dispersions (point 7) and bring the booster from its current position and velocity to a soft touchdown at the drone ship (point 8). The ability to cope with dispersions during recovery leads to the need for closed-loop guidance techniques, where guidance commands are computed in real-time to correct the trajectory based on onboard measurements. All the computations are made in the RP frame and the required thrust vector in this frame is then converted back to $\{\theta_{\text{ref}}(t),\, \psi_{\text{ref}}(t)\}$ and $T_{\text{ref}}(t)$.

Furthermore, for a more efficient management of aerothermal requirements, recovery guidance can be explicitly divided into three phases: (i) a re-entry burn aimed at decelerating the booster, (ii) a second engine cut-off and (iii) a landing burn that ensures a precise touchdown. In addition, as depicted in Fig. 5a, the reusable stage needs to undergo a slow but significant change in attitude between points 4 and 6. This flip-over manoeuvre is simulated by a change in pitch with constant rate executed using fins and cold gas thrusters.

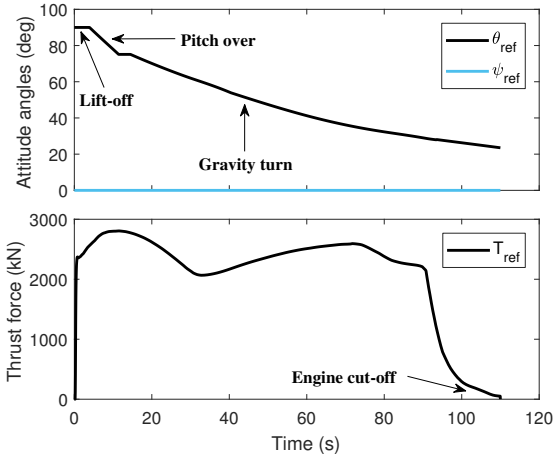

Fig. 6 Ascent attitude and thrust references

As an alternative recovery solution, the reusable booster can use its main engine not only for deceleration and landing, but also to deliver an additional burn that brings it to a recovery pad close to the launch site. The additional firing naturally leads to a more demanding propellant consumption, which can be nonetheless paid for by avoiding the use of a sea-going platform and all the associated infrastructure and operational costs. This recovery strategy is known as return to launch site (RTLS) and is illustrated in Fig. 5b.

Until separation (i.e. point 4), the RTLS and DRL missions have the same profile, which is therefore omitted in Fig. 5b for clarity. From this point forward, as introduced above, the reusable stage needs to perform a rapid flip-over manoeuvre (point 5) followed by the boostback burn (point 6) in the direction of the launch site. Following the boostback cut-off (point 7), the rest of the recovery (from point 8 onwards) is similar to DRL: an exo-atmospheric flight where the booster flips over at a slower rate, a closed-loop recovery stage that starts at h_s (and is achieved with one or two distinct burns), and finally a soft touchdown.

In the RTLS scenario, the flip-over manoeuvres are again executed by fin and thruster induced pitch variations with constant rate. In addition, for this study, the boostback burn is fixed to an open-loop firing with magnitude $T_{\text{ref}} = 600$ kN, direction $\{\theta_{\text{ref}}, \psi_{\text{ref}}\} = \{180, 0\}$ degrees and duration 30 seconds.

Finally, it is important to mention that closed-loop guidance techniques for powered descent and landing are generally independent of the type of recovery strategy – since all the computations are made in the RP frame, the only difference lies on the definition of this frame and of the corresponding transformation $C_{\mathbf{q}_R^E}$. The baseline technique adopted in this study is presented the following subsection.

B. Constrained Terminal Velocity Guidance

Constrained terminal velocity (CTV) guidance has its roots in the missile interception problem [20, 21], but it has been successfully applied also to asteroid intercept and landing [22–26]. The main strength of this technique lies on its simplicity, which makes it extremely easy to implement and allows to have a rough idea of recovery flight mechanics very quickly.

CTV guidance is based on the compensation of *zero-effort-miss* and *zero-effort-velocity* vectors, $\mathbf{ZEM}(t)$ and $\mathbf{ZEV}(t)$, which quantify the position and velocity error at the end-of-mission if no corrective manoeuvres are made after time t. Using these coordinates, the required thrust vector is given in the RP frame by:

$$\mathbf{T}_{\mathrm{CTV}}(t) = \hat{m}(t) \begin{bmatrix} k_r & k_v \end{bmatrix} \begin{bmatrix} \dfrac{\mathbf{ZEM}(t)}{(t_f - t)^2} \\ \\ \dfrac{\mathbf{ZEV}(t)}{t_f - t} \end{bmatrix} \tag{47}$$

This computation requires an estimate of the vehicle's mass $\hat{m}(t)$ and the specification of the end-of-mission (i.e. touchdown) time t_f. Optimal values of $\{6,\ -2\}$ for the two gains $\{k_r,\ k_v\}$ have been derived in [23, 24] by recasting the problem as a fuel-optimal trajectory generation problem with constrained boundary position and velocity and assuming a uniform and well-known gravity field, which is a valid approximation for the Earth.

The estimation of $\mathbf{ZEM}(t)$ and $\mathbf{ZEV}(t)$ involves propagating the equations of motion from t to t_f, which can become computationally challenging without some approximations. The accuracy of the guidance law naturally depends on how conservative those approximations are. This subsection seeks the simplest possible law and hence, neglecting (i) gravity variations during descent, (ii) mass variations due to propellant consumption, (iii) aerodynamic forces, and (iv) non-inertial effects of the RP frame, then the zero-effort errors correspond to:

$$\mathbf{ZEM}(t) = \mathbf{r}_f - \left[\hat{\mathbf{r}}(t) + (t_f - t)\,\hat{\mathbf{v}}(t) + \frac{1}{2}(t_f - t)^2\,\hat{\mathbf{g}}(t)\right] \tag{48}$$

$$\mathbf{ZEV}(t) = \mathbf{v}_f - \left[\hat{\mathbf{v}}(t) + (t_f - t)\,\hat{\mathbf{g}}(t)\right] \tag{49}$$

where $\mathbf{r}_f = \mathbf{v}_f = [0;\ 0;\ 0]$ for a soft landing at the recovery pad, $\hat{\mathbf{r}}(t)$ and $\hat{\mathbf{v}}(t)$ are estimates in the RP frame as per Eq. (2) and $\hat{\mathbf{g}}(t)$ is computed applying the same rotation to Eq. (5).

Care must also be taken in Eq. (47) to avoid a singularity when $t \to t_f$. The most effective way to do this is by switching-off the guidance commands immediately before the end-of-mission. The exact instant of time represents a trade-off between allowable touchdown error and maximum thrust authority.

Due to its simplicity, the computational time required by the CTV algorithm is extremely low, so guidance commands can be updated at the same frequency of the simulation, $f_{\mathrm{gui}} = f_{\mathrm{sim}} = 10$ Hz, starting at a pre-specified altitude h_{s}. It is

also rather useful to quickly assess the performance impact of different design choices.

Nevertheless, the inherent capabilities of CTV guidance are also rather limited. The most relevant limitation lies on its inability to explicitly enforce path constraints (i.e. only boundary states can be constrained). Path constraints may be applied to the states (e.g. aerothermal loads and subsurface flight avoidance) as well as to the control inputs (e.g. lower and upper throttling magnitude and rate limits) and both of them are critical for RLV recovery. For this reason, more sophisticated algorithms such as those based on convex optimisation are being developed [9, 27]. In the present article, aerodynamic and thermal load constraints are considered only through simulations.

IV. RLV Control Approach

This section exemplifies the manner attitude control algorithms can be designed and integrated in the RLV benchmark. A model often employed for preliminary launcher calculations (e.g. [28–30]) is used for this demonstration. The standard simplifying assumptions for launcher attitude control are considered in here, i.e. axis-symmetric vehicle and not accounting for roll perturbations, drift, angle of attack and wind effects.

The model representing the rotational dynamics under the presence of aerodynamic effects [10] is given in the frequency-domain for a certain instant of time t as:

$$\frac{\theta\,(\mathrm{s})}{m_{\mathrm{ctr}}\,(\mathrm{s})} = \frac{1}{\mathrm{s}^2 - \mu_{\alpha'}(t)} \tag{50}$$

In the equation, $\theta(\mathrm{s})$ represents pitch deviations relative to a certain trim state, $m_{\mathrm{ctr}}(\mathrm{s})$ represents specific pitch control moment divided by the lateral moment of inertia and $\mu_{\alpha'}(t)$ is the load-proneness parameter introduced in Eq. (33).

The high-level objective of any launcher's attitude control system is to stabilise the dynamics of Eq. (50) and track commands $\theta_{\mathrm{ref}}(\mathrm{s})$ provided by the guidance module, which can be achieved classically using a proportional-derivative (PD) controller. The architecture of the adopted PD controller is depicted in Fig. 7, with the PD gains $k_{\mathrm{p}}(t)$ and $k_{\mathrm{d}}(t)$ shown as time-varying due to $\mu_{\alpha'}(t)$. Angular errors are measured based on orientation of the body-fixed frame with respect to the LP frame (recall Sec. II.A), which requires the knowledge of $C_{\mathbf{q}_{\mathrm{E}}^{\mathrm{L}}}$, $C_{\mathbf{q}_{\mathrm{I}}^{\mathrm{E}}}(t)$ and $C_{\mathbf{q}_{\mathrm{B}}^{\mathrm{I}}}(t)$. Note that a first-order derivative filter with time constant $\sigma_{\mathrm{d}} = 0.2$ seconds is used to calculate the the reference pitch rate command.

Figure 7 also shows a "control allocation" block that relates the specific control moment $m_{\mathrm{ctr}}(\mathrm{s})$ to the actual RLV control inputs $\beta_{\mathrm{TVC,y}}(\mathrm{s})$, $\beta_{\mathrm{fin,y}}(\mathrm{s})$ and $\beta_{\mathrm{thr,y}}(\mathrm{s})$, with $\beta_{\mathrm{fin,y}}(\mathrm{s}) = \beta_{\mathrm{fin},1}(\mathrm{s}) = \beta_{\mathrm{fin},2}(\mathrm{s})$ for the pitch channel. Using the control effectiveness coefficients defined in Eqs. (24), (32) and (36), this relation is conveniently expressed as:

$$m_{\mathrm{ctr}}\,(\mathrm{s}) = -\begin{bmatrix}\mu_{\mathrm{c}}(t) & \mu_{\mathrm{f}}(t) & \mu_{\mathrm{t}}(t)\end{bmatrix}\begin{bmatrix}\beta_{\mathrm{TVC,y}}\,(\mathrm{s})\\ \beta_{\mathrm{fin,y}}\,(\mathrm{s})\\ \beta_{\mathrm{thr,y}}\,(\mathrm{s})\end{bmatrix} \tag{51}$$

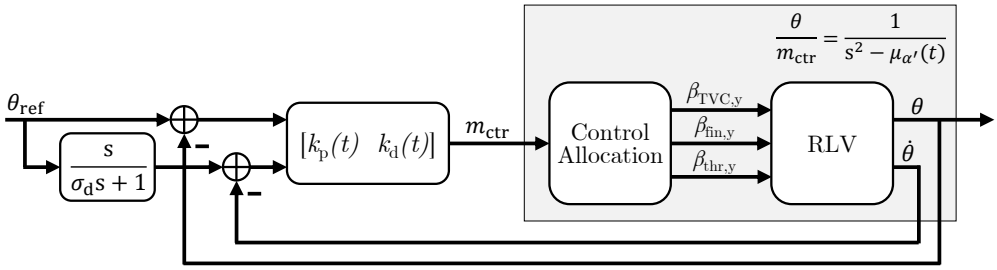

Fig. 7 Closed-loop attitude control model (pitch channel)

The role of control allocation is to compute the inverse of this (overdetermined) equation in a way that is suitable for the different phases of L&R flight.

A. Preliminary Control Design

Equation (50) is time (and trajectory) dependent through $\mu_{\alpha'}(t)$, which determines its poles: they are placed at $\pm\sqrt{\mu_{\alpha'}(t)}$ when $\mu_{\alpha'}(t) > 0$ and at $\pm j\sqrt{\mu_{\alpha'}(t)}$ otherwise. Since $\mu_{\alpha'}(t)$ is a combination of the aerodynamic contributions of $\mu_\alpha(t)$ and $\mu_{\mathrm{f}}(t)$, it is also interesting to look at their individual effects, as well as at the contribution of $\mu_{\mathrm{c}}(t)$ and $\mu_{\mathrm{t}}(t)$.

Figure 8a shows the estimates of $\sqrt{\mu_*(t)}\,\mathrm{sgn}\mu_*(t)$, with $* = \{\alpha,\ \mathrm{f},\ \alpha',\ \mathrm{c}\}$, throughout a closed-loop DRL trajectory. In the case of $\mu_{\alpha'}(t)$ and $\mu_\alpha(t)$, this corresponds to the natural frequency of the poles with and without fins; positive values indicate open-loop instability and non-positive values indicate marginal stability. The figure was obtained in an iterative manner since changes on control parameters affect the trajectory, but changes on the trajectory affect the effectiveness levels and consequently the control parameters.

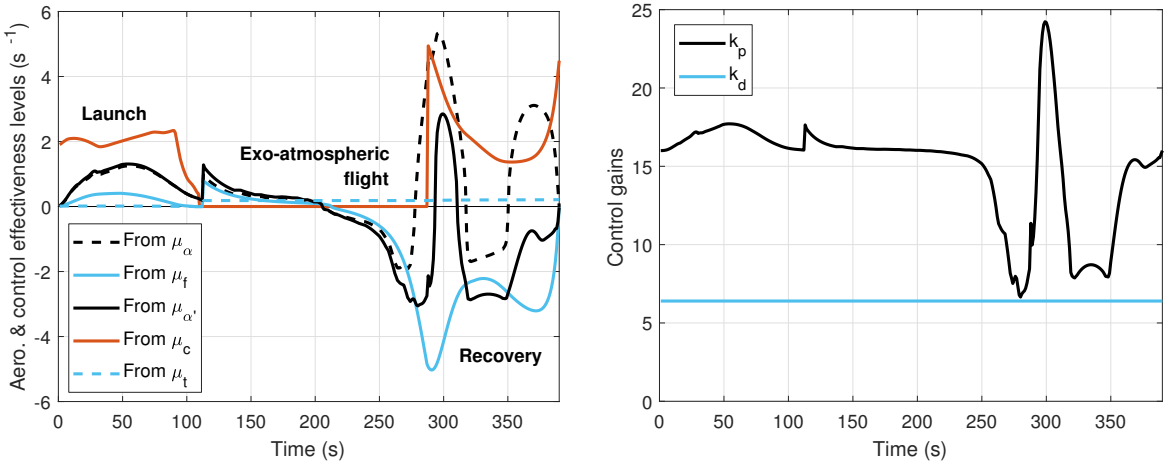

(a) Aerodynamic and control effectiveness levels

(b) Control gains

Fig. 8 Stability and control results for DRL trajectory

The evolution of the $\mu_\alpha(t)$ indicator shows that an RLV with no fins would be open-loop unstable for the first half of the DRL trajectory (until the pitch angle becomes larger than 90 degrees, at around 200 seconds) and for most of the second half. In addition, narrow areas of marginal stability between the time regions of [200, 270] and [320, 350] seconds are seen in Fig. 8a. They can be related to a combination of $C_{N_\alpha}(t) < 0$ and $x_{\mathrm{CP}}(t) > x_{\mathrm{CG}}(t)$. The magnitude of the $\mu_{\mathrm{f}}(t)$ indicator follows that of $\mu_\alpha(t)$ due to their common dependence on $Q(t)/J_N(t)$, but its sign has a more monotonic variation due to $C_{\mathrm{fin}_\alpha}(t)$ being strictly positive for the first half and negative for the second.

Hence, $\mu_{\alpha'}(t)$ confirms that the chosen fins have very little impact during launch, but they do provide a significant stability improvement for recovery and landing with $\mu_{\alpha'}(t) << \mu_\alpha(t)$ – the most challenging area is around 300 seconds and coincides with re-entry and first stage re-ignition as will be seen later. In addition, $\mu_{\alpha'}(t)$ is always considerably inferior to both $\mu_{\mathrm{c}}(t)$ and $\mu_{\mathrm{f}}(t)$ in absolute value so that a margin for stability and control is ensured. The only exception is the exo-atmospheric flight phase, during which cold gas thrusters with effectiveness $\mu_{\mathrm{t}}(t)$ have to be employed.

The closed-loop transfer function of Fig. 7 is then given by:

$$\frac{\theta\,(\mathrm{s})}{\theta_{\mathrm{ref}}\,(\mathrm{s})} = \frac{\Big(k_{\mathrm{d}}(t) + \sigma_{\mathrm{d}}\,k_{\mathrm{p}}(t)\Big)\mathrm{s} + k_{\mathrm{p}}(t)}{\Big(\sigma_{\mathrm{d}}\,\mathrm{s} + 1\Big)\Big(\mathrm{s}^2 + k_{\mathrm{d}}(t)\,\mathrm{s} + k_{\mathrm{p}}(t) - \mu_{\alpha'}(t)\Big)} \tag{52}$$

and can be easily employed to choose the gains $k_{\mathrm{p}}(t)$ and $k_{\mathrm{d}}(t)$ via pole-placement. Here, this is carried out so as to have a constant natural frequency and damping ratio of the 2nd order term in the denominator throughout the trajectory (with the other term solely defined by σ_{d}). Once again, this is a simplification for illustration purposes and does not represent the industrial state-of-practice, where the required attitude tracking performance changes with the phase of flight. For example, tracking performance should be less demanding at high dynamic pressure [31] and more demanding for landing. The control gains required for a constant natural frequency of 4 rad/s and damping ratio of 0.8 are depicted in Fig. 8b.

As mentioned before, the same process is followed for yaw attitude control design. There are however two main differences that must be pointed out. The first one is related to the fact that, as there is no flip-over manoeuvre in the yaw channel, there is no sign reversal of the fin effectiveness $\mu_{\mathrm{f}}(t)$ (recall Fig. 8a) to be taken into account for the computation of $\beta_{\mathrm{fin,z}}$ from Eq. (51). The second remark is that fins in the yaw plane will also be employed to compensate for any roll rate perturbation $\dot{\phi}$. This is achieved by adding extra differential deflections as follows:

$$\begin{cases} \beta_{\mathrm{fin},3} = \beta_{\mathrm{fin,z}} + k_\phi\,\dot{\phi} \\ \beta_{\mathrm{fin},4} = \beta_{\mathrm{fin,z}} - k_\phi\,\dot{\phi} \end{cases} \tag{53}$$

Here, k_ϕ is assumed constant and equal to 0.1 seconds for the sake of simplicity. Although fin effectiveness is not uniform throughout the trajectory, this roll-rate stabilisation strategy is proven very successful for this study.

B. Control Allocation

For this study, the commanded control moment $m_{\text{ctr}}(t)$ is allocated between the three effectors (TVC, fins and cold gas thrusters) using a simple algorithm based on [32]. The main idea is to try allocating $m_{\text{ctr}}(t)$ entirely to a primary effector ϵ_1 and only employ a secondary effector ϵ_2 if the maximum authority of the primary effector $\bar{\beta}_{\epsilon_1}$ were to be exceeded. Following the notation above and the definition of Eq. (51), control inputs are first computed as:

$$\beta_{\epsilon_1}(t) = -\frac{m_{\text{ctr}}(t)}{\mu_{\epsilon_1}(t)}, \qquad \beta_{\epsilon_2}(t) = 0 \tag{54}$$

Then, if the maximum authority of ϵ_1 is exceeded, i.e. if $|\beta_{\epsilon_1}(t)| > \bar{\beta}_{\epsilon_1}$, $\beta_{\epsilon_1}(t)$ is constrained and $\beta_{\epsilon_2}(t)$ is updated as follows:

$$\beta_{\epsilon_1}(t) = \bar{\beta}_{\epsilon_1} \operatorname{sgn} \beta_{\epsilon_1}(t), \qquad \beta_{\epsilon_2}(t) = -\frac{m_{\text{ctr}}(t) + \mu_{\epsilon_1}(t)\,\beta_{\epsilon_1}(t)}{\mu_{\epsilon_2}(t)} \tag{55}$$

where the numerator of $\beta_{\epsilon_2}(t)$ corresponds to the difference between the commanded moment and the one achievable with ϵ_1.

A suitable definition of primary and secondary effectors naturally changes throughout the trajectory according to their effectiveness coefficients. The choice implemented in the present study is summarised in Table 3.

Table 3 Control allocation modes

	Primary effector	Secondary effector
From lift-off to engine cut-off (t = 110 s)	TVC	—
From previous to PL separation (t = 112 s)	*open-loop*	—
From previous to drop of $\lvert\mu_{\text{f}}(t)\rvert$	Fins (35 deg max)	Thrusters
From previous to recovery of $\lvert\mu_{\text{f}}(t)\rvert$	Thrusters	—
From previous to t_f with: low thrust	Fins (35 deg max)	TVC
high thrust	TVC (3 deg max)	Fins

As the table shows, 6 modes have been defined, and for each a maximum authority value of the primary effector can be assigned. Note that there are a couple of modes where no secondary effector is necessary. In addition, the few seconds prior to PL separation are performed in open-loop so as to avoid instability caused by the rapid change of inertia.

V. Coupled Assessment

The assessment of coupled flight mechanics and G&C laws will be demonstrated in this section in two ways. First, a detailed comparison of DRL and RTLS missions using the CTV recovery guidance and a perfect attitude control is given. Then, the impact of attitude control on the stability and performance of DRL missions is assessed.

A. Recovery Analysis

The aim in this section is to provide a quantitative comparison between DRL and RTLS recovery strategies. Since the main differences between these missions are mostly related to their trajectory, perfect attitude control dynamics will be assumed for simplicity. This means that attitude angles are exactly what they are commanded to be, $\{\theta(t), \psi(t)\} = \{\theta_{\text{ref}}(t), \psi_{\text{ref}}(t)\}$, and that all the aerodynamic moments generated by the vehicle are compensated for, $\mathbf{M}_{\text{aero}}(t) + \mathbf{M}_{\text{TVC}}(t) + \mathbf{M}_{\text{fins}}(t) + \mathbf{M}_{\text{thr}}(t) = 0$. This is the standard approach used when developing and assessing guidance schemes.

The two L&R trajectories obtained with CTV guidance triggered at $h_s = 25$ km are depicted in Fig. 9. Although sharing the same launch profile, the distinction between downrange landing (DRL) using the sea-going recovery platform with final time $t_f = 390$ seconds and return to launch site (RTLS) with $t_f = 500$ seconds is clear in the figure. These choices were made based on a detailed performance trade-off analysis between required propellant, dynamic pressure and touchdown velocity for different re-ignition altitudes, mission durations and single/double boost alternatives. This analysis is available in [9].

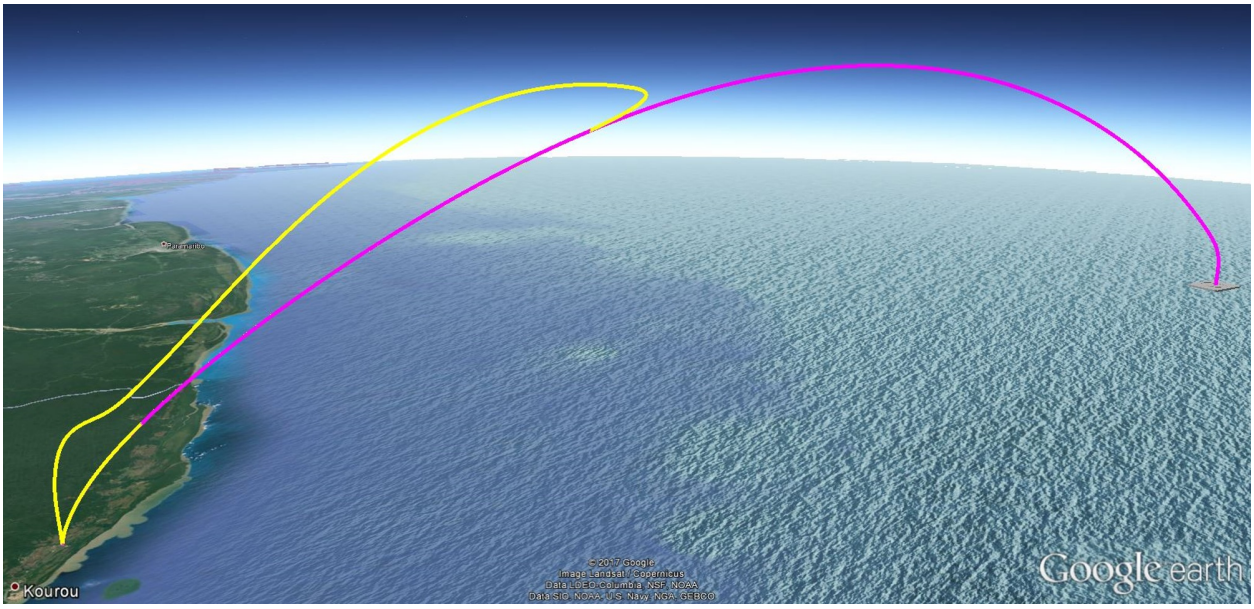

Fig. 9 DRL and RTLS trajectories (©2017 Google, `https://www.google.com/earth/`)

Detailed results of the simulations are plotted in Fig. 10 for DRL and Fig. 11 for RTLS. The phases of launch (from lift-off to separation), exo-atmospheric flight (from separation to recovery burn) and recovery (from recovery burn to touchdown) are distinguished in every plot using dash-dotted, dashed and continuous lines respectively, and a thorough analysis of the plots is provided subsequently.

The figures show the most relevant flight performance indicators, also gathered in Table 4. These indicators include total propellant consumption m_{burnt} given as a percentage of its initial value $m_{\text{prop}}(0)$, maximum aerothermal loads, Q and Q_H, vertical and horizontal touchdown velocity, $\|\mathbf{v}_{\text{R}_z}(t_f)\|$ and $\|\mathbf{v}_{\text{R}_{x,y}}(t_f)\|$, as well as position error $\|\mathbf{r}_{\text{R}_{x,y}}(t_f)\|$.

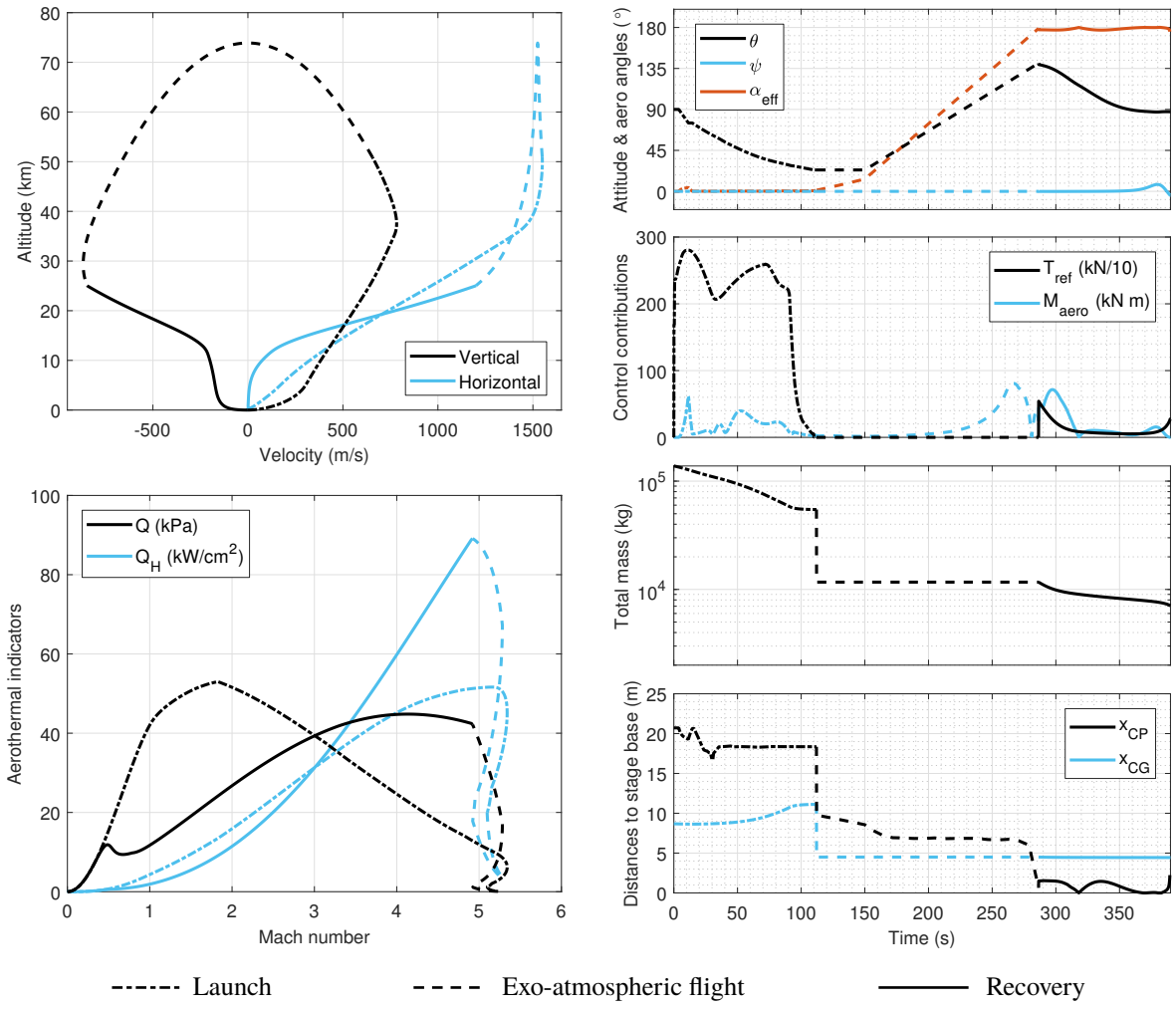

Fig. 10 DRL flight mechanics results

The top-left plot of Fig. 10 shows the evolution of vertical and horizontal velocity as a function of altitude (in the vertical axis) for the DRL scenario. During launch, velocity increases in both vertical and horizontal directions and separation occurs when the latter reaches its maximum value at an approximate altitude of 51 km. From that point, the vehicle continues to ascent until its vertical velocity becomes zero at an approximate altitude of 74 km and then starts to accelerate downwards due to the action of gravity. In the meantime, horizontal velocity is dissipated as a consequence of aerodynamic forces, which become more intense as altitude decreases (and air density increases). Then, at 25 km, recovery guidance is activated and the commanded burn brings both components to zero at the landing point. It is important to notice that horizontal velocity converges to this value significantly before their counterpart, which is critical to ensure a vertical landing.

The bottom-left plot illustrates the evolution of dynamic pressure (Eq. (10)) and heat flux (Eq. (20)) as a function of the vehicle's Mach number. During launch, velocity increases and air density decreases, which causes Q and Q_H to tend to zero at lift-off and at maximum altitude (where $M \approx 5.3$) and to have a peak value in-between. These indicators

then increase abruptly once the RLV plunges downwards (at $M \approx 4.9$) and re-enters the atmosphere. At this point, recovery guidance is activated in order to manage the second peak value of these indicators and bring it to zero at the landing point. Maximum values of Q and Q_H during L&R are registered in Table 4.

The uppermost plot on the right-hand side of Fig. 10 shows the reference pitch and yaw angles $\{\theta_{\text{ref}}, \psi_{\text{ref}}\}$ as well as the total angle of attack α_{eff} over mission time. The reference attitude angles were shown in Fig. 6 for the launch phase. In terms of the angle of attack, it remains close to zero during this phase, with a maximum value under 5 degrees around pitch over (at 10 seconds). Subsequently, the reference pitch angle follows a constant-rate manoeuvre to flip over the booster during the exo-atmospheric flight while demanding a constant yaw angle. This constant-rate flip over manoeuvre causes the angle of attack to go from zero to 180 degrees, which implies that the velocity vector becomes aligned with the booster's base. And finally during the recovery, the reference attitude angles are computed by the guidance algorithm, which results in θ_{ref} converging to 90 degrees at touchdown (ensuring a vertical landing), ψ_{ref} remaining close to zero due to little aerodynamic couplings with the pitch motion and α_{eff} close to 180 degrees.

The second right-hand plot illustrates the evolution of the thrust vector magnitude T_{ref} and aerodynamic moment $||\mathbf{M}_{\text{aero}}||$. Similar to the previous plot, T_{ref} is given by Fig. 6 during the launch phase and computed by the guidance algorithm during recovery. The recovery burn is more intense at the beginning (where zero-effort errors are larger) and close to touchdown (where $t \to t_f$). The aerodynamic moment to be compensated, as expected, is more demanding in zones of high dynamic pressure and angle of attack.

The third right-hand plot of Fig. 10 shows the evolution of the vehicle's total mass using logarithmic scale for clarity. Here, three zones of mass variation can be identified: (i) launch burn, where most of the propellant is depleted, (ii) separation (sudden drop of m_{PL} at 112 seconds of flight), and (iii) recovery burn for re-entry and landing. Propellant consumption during L&R is also registered in Table 4 with respect to its initial mass. In this scenario, while 90.30% of propellant is depleted during launch, only 4.98% is required for the recovery, which leaves a margin of about 4.7%.

Finally, the bottom-right plot illustrates the longitudinal travel of CP and CG relative to the booster's base throughout the flight. While the former is governed by the aerodynamic environment encountered, the latter follows the depletion of mass as per Eq. (42). Hence, the same three zones of launch (with CG moving forward), separation (sudden drop of m_{PL} h_{PL}) and recovery (CG moves backward, although not visible in the plot as mass variation is quite small) can be distinguished. In any case, the RLV is inherently unstable during powered flight since the CP is located in front of the CG during ascent and behind during descent.

Regarding the RTLS results provided in Fig. 11, the main difference with respect to the previous scenario lies on the boostback burn required to bring the stage back to the launch site. In terms of velocity (top-left plot), this burn results in the inversion of the horizontal component and the reduction of its magnitude to approximately half of its value at separation. In addition, there is a stronger interplay between vertical and horizontal components, also visible in Fig. 9, caused by the close interactions between trajectory and aerodynamics that are not taken into account by the

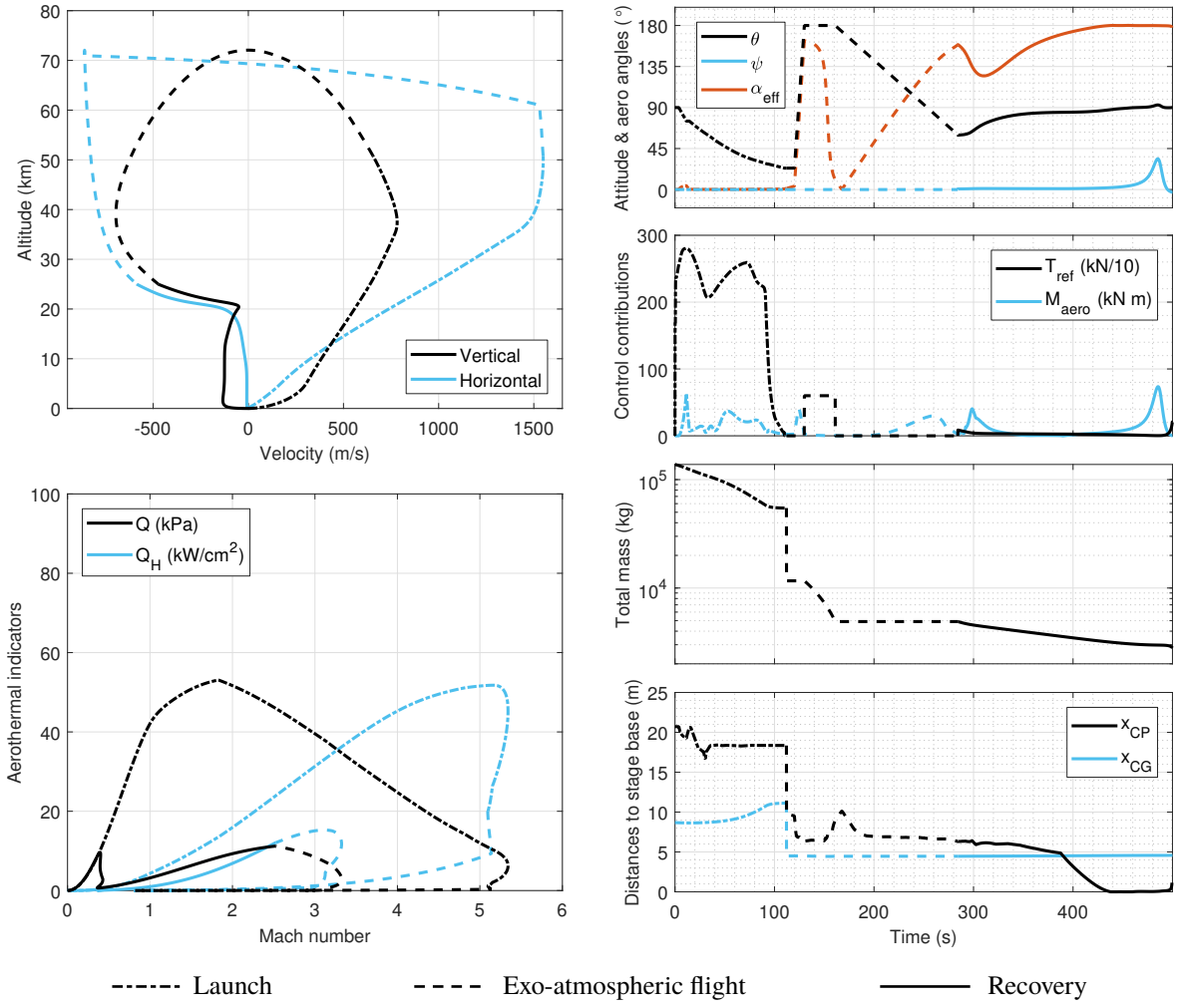

Fig. 11 RTLS flight mechanics results

CTV algorithm. This was one of the drawbacks identified before for this type of guidance. The velocity reduction is then translated into less demanding aerothermal recovery indicators than for the DRL trajectory, as evidenced by the bottom-left plot and in Table 4.

In terms of attitude (top-right plot of Fig. 11), the main difference is related to the rapid constant-rate flip over manoeuvre, followed by a 30 seconds period with constant pitch $\theta_{\text{ref}} = 180$ degrees during which the boostback burn takes place (recall Fig. 5b) and by a second constant-rate manoeuvre prior to the recovery burn. The flip over manoeuvre also causes the total angle of attack to follow the pitch variation, but the former angle returns to zero as soon as the horizontal velocity is inverted by the boostback burn. Once the recovery burn is activated, the observations are similar to the DRL approach, although the coupling between pitch and yaw motion is slightly more intense.

The thrust reference associated with the boostback burn is clearly visible in the second right-hand plot. The velocity reduction this burn induces is reflected into less intense thrust commands during recovery compared to the DRL scenario, but larger aerodynamic moments due to higher angles of attack. Also as a result of this burn, an additional

mass-depletion zone is visible in the third right-hand plot. The evolution of CP and CG in the bottom-right plot is also slightly different in comparison with the DRL case, but the overall observations are the same.

Table 4 Nominal L&R performance indicators

Indicator	Launch	DRL	RTLS
$m_{\text{burnt}}(t_f)/m_{\text{prop}}(0)$ (%)	90.3	4.98	9.60
max Q (kPa)	53.0	44.8	11.2
max Q_H (kW/cm^2)	51.7	89.1	15.3
$\|\|\mathbf{v}_{\mathrm{R}_z}(t_f)\|\|$ (m/s)	—	0.39	1.34
$\|\|\mathbf{v}_{\mathrm{R}_{x,y}}(t_f)\|\|$ (m/s)	—	1.24	1.19
$\|\|\mathbf{r}_{\mathrm{R}_{x,y}}(t_f)\|\|$ (m)	—	0.01	0.08

Despite the less intense effort during recovery, the boostback burn makes the RTLS approach a significantly more demanding trajectory in terms of propellant consumption (see Table 4). In fact, 9.6% of propellant is now required for the recovery, leaving a margin of only 0.1%. This very tight margin motivates the need for more performing recovery guidance algorithms. A follow-up investigation on improving the performance of the present baseline algorithm is provided in [9].

In addition to the indicators already covered, Table 4 includes vertical and horizontal touchdown velocity, as well as position error, which are naturally of critical relevance for recovery assessment. For the two cases analysed, all these values are well within an adequate range. It is highlighted that these indicators should be ideally as small as possible but, in practice, their combined optimisation is an extremely challenging activity. The reason behind this is that a choice of recovery guidance tuning parameters that minimises propellant consumption is likely to subject the vehicle to higher aerothermal loads and touchdown errors, and vice-versa.

Finally, to analyse the practical feasibility of the proposed guidance approach, 1000 Monte-Carlo runs of the DRL recovery were performed with wind gusts perturbing both ascent and descent phases. These gusts are introduced using two orthogonal components w_{NRN} and w_{ERN} (recall Eq. (6)) and modelled by uncorrelated Dryden filters. These filters are scheduled as a function of altitude and airspeed, and parametrised for light, moderate and severe levels of wind (for further information on the application of Dryden filters to launcher flight control, the reader is referred to [29, 31]).

The final landing trajectories and touchdown position/velocity dispersions obtained with severe wind are provided in Fig. 12a and 12b, respectively. These figures show that all the wind-induced dispersions could be shrunk towards successful pinpoint soft landings. As highlighted in Fig. 12b, the touchdown position has a 3σ dispersion of 0.1 m around the recovery platform's centre and less than 1% of the cases landed with velocity higher than 3.5 m/s.

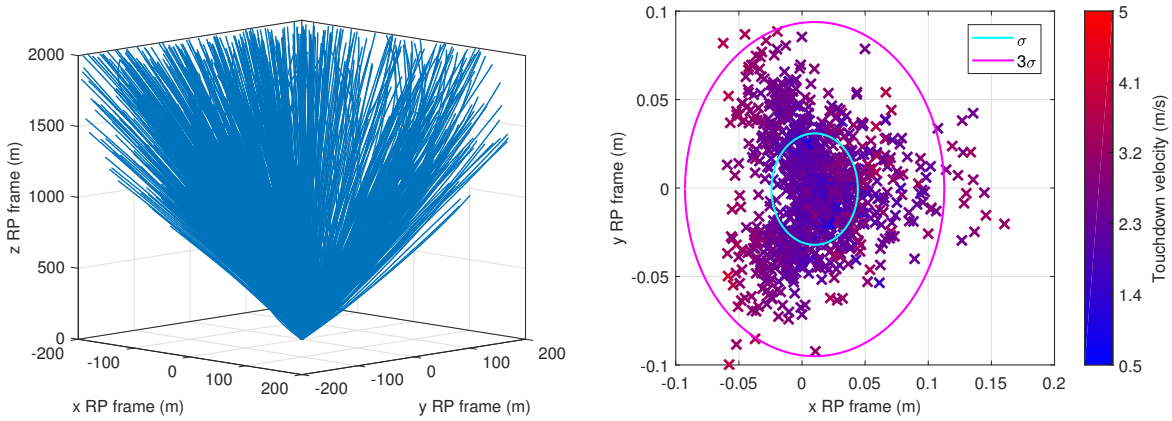

(a) Landing trajectories in the RP frame

(b) Position and velocity dispersions at touchdown

Fig. 12 DRL results of 1000 Monte-Carlo runs with severe wind

B. Controllability Analysis

The impact of attitude control on L&R trajectories is now addressed by closing the loop with the controller introduced in Sec. IV and using the time-scheduled control gains of Fig. 8b. This section focuses on DRL missions since they were shown to be the most demanding ones in terms of aerothermal loads (recall Table 4). As in the previous section, only rigid-body motion is considered. Detailed simulation results are depicted in Fig. 13.

The two left-hand side plots in Fig. 13 show the same information as Fig. 10 (i.e. velocity components vs. altitude and aerothermal indicators vs. Mach), but without distinguishing now the phases of flight. It can be seen that general trends and peak values with respect to the previous perfect control DRL trajectory are extremely similar. The main differences take place close to touchdown, where the evolution of vertical and horizontal velocity becomes slightly more elaborate. This happens because descent guidance and attitude control are tightly coupled: actuator deflections required for attitude control generate lateral forces as a side effect, which then cause landing trajectory and guidance commands to change. This coupling is actually one of the most challenging issues for launcher stage recovery and the main motivation for the work of this study.

The uppermost plot on the right-hand side of Fig. 13 shows now the evolution of commanded and actual attitude angles. It is clear that the pitch and yaw commands are successfully tracked (with larger errors during re-entry and first stage re-ignition) while roll is kept approximately constant throughout the mission. It is also interesting to verify that the commands are quite different from those in Fig. 10 due to the aforementioned guidance-control coupling.

The required actuator deflections are provided in the second right-hand plot for TVC and in the last plot for the fins. The main critical events are also identified in both plots. Cold gas thrusters are only active during the designated area and not shown for the sake of conciseness. Evolution of the main engine thrust magnitude and vehicle MCI properties are similar to those of Fig. 10 and therefore also omitted.

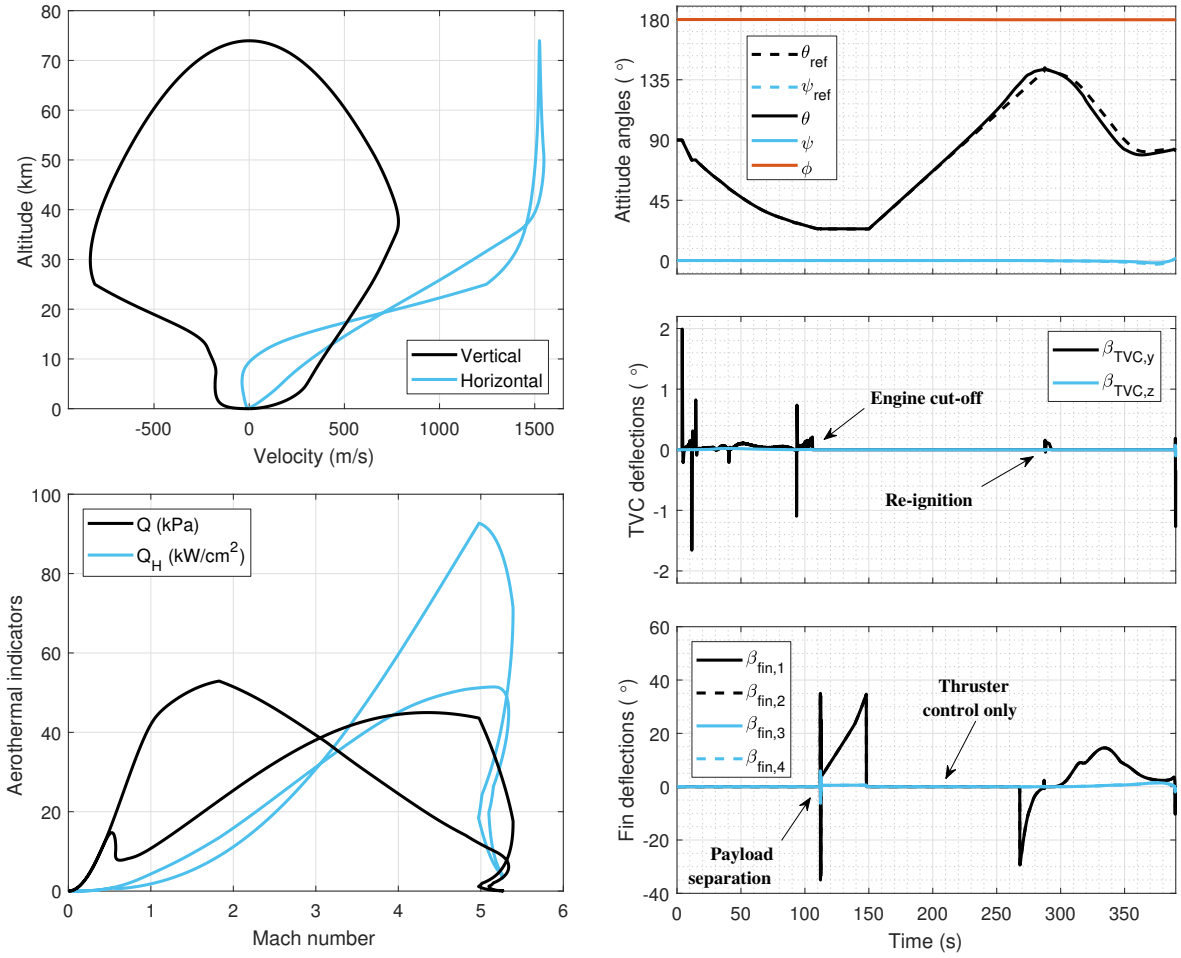

Fig. 13 Closed-loop DRL results

As these two last right-hand plots show, attitude is controlled using TVC only (with maximum deflection of 2 degrees) until engine cut-off. This is followed by a few seconds of open-loop control (recall Table 3) and by fin activation to compensate for perturbations related to PL separation and high-speed aerodynamics. There is then a period of thruster control only where fin effectiveness is reduced due to the high altitude. Finally, fins are reactivated for precise control during descent and landing, and are also aided by the TVC when its effectiveness is higher, at the start and end of recovery burn. Naturally, the majority of control activity takes place in the trajectory pitch plane (through $\beta_{\text{TVC,y}}$, $\beta_{\text{fin},1}$ and $\beta_{\text{fin},2}$) and the remaining deflections are mostly employed for small corrections. It is important to highlight that, while $\beta_{\text{fin},1} = \beta_{\text{fin},2}$, the same does not hold for $\beta_{\text{fin},3}$ and $\beta_{\text{fin},4}$ due to their differential deflection for roll stabilisation given by Eq. (53). This difference is in the order of 10^{-3} degrees and therefore not visible in the plot.

The information provided by these simulations is also crucial at the vehicle's sizing stage as it allows to evaluate the control authority that is required to ensure its controllability over the flight and under different levels of wind perturbations. For instance, one can compute trim conditions of the lateral motion throughout the trajectory based on the equilibrium of moments with respect to the body $\mathbf{j}_{\text{B}}$ or $\mathbf{k}_{\text{B}}$ axes.

The aforementioned conditions correspond to the solution of $M_{\text{aero}}(t) + M_{\text{TVC}}(t) + M_{\text{fins}}(t) = 0$ which, using the nomenclature of Sec. II, is defined as:

$$S_{\text{ref}} \left[x_{\text{CP}} - x_{\text{CG}}\right] C_N \left(\alpha, M\right) = \frac{T_{\text{ref}}}{Q} \left[x_{\text{CG}} - x_{\text{PVP}}\right] \sin \beta_{\text{TVC,y}} + 2 S_{\text{fin}} \left[x_{\text{fin}} - x_{\text{CG}}\right] C_{\text{fin}} \left(\beta_{\text{fin,y}} - \alpha\right) \cos \beta_{\text{fin,y}} \tag{56}$$

where dependencies on t have been dropped for simplicity and $C_N \left(\alpha, M\right)$ and $C_{\text{fin}} \left(\beta_{\text{fin,y}} - \alpha\right)$ are given by Eq. (19) and (27). Moreover, wind perturbations of velocity v_w in the vehicle's normal axis are introduced via angle of attack perturbations as follows:

$$\tan \alpha = \frac{v_{\text{air,z}} - v_w}{v_{\text{air,x}}} = \tan \alpha_0 - \frac{v_w}{\|\mathbf{v}_{\text{air}}\| \cos \alpha_0} \tag{57}$$

in which α_0 is the value taken from the simulation with no wind. The impact of such perturbations changes greatly throughout the trajectory and this can be quantified using the Q_α indicator introduced in Sec. II.C. The time responses of this indicator during the simulation of Fig. 13 and for different values of $v_w \in [-15, 45]$ m/s around that trajectory are provided (using different colours) in Fig. 14.

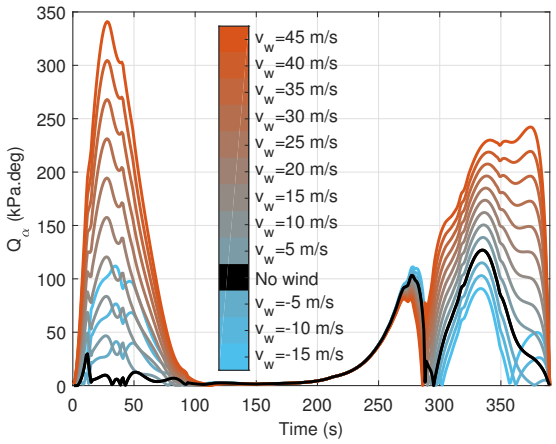

Fig. 14 Impact of wind on closed-loop DRL Q_α

As this figure shows, there is one main Q_α peak during launch and another one during recovery. These peaks are worsened when $v_w \neq 0$ in accordance with Eq. (57). The impact of wind is higher for launch, but the nominal Q_α peak is more demanding for recovery, both of them caused by the fact that α_0 is also higher at recovery than at launch.

Trim curves are then plotted in Fig. 15a and 15b for two extreme conditions during recovery: booster re-ignition (at 288 seconds) and maximum Q_α (at 335 seconds), respectively. Each plot shows solutions of Eq. (56) for fin deflections $|\beta_{\text{fin,y}}| \leq 40$ degrees (x axis), TVC deflections $|\beta_{\text{TVC,y}}| \leq 15$ degrees (y axis) and wind perturbations v_w.

From Fig. 15a, it is possible to observe that, in spite of the dynamic disturbance induced by the booster re-ignition at 288 seconds, controlling the vehicle is not particularly demanding nor affected by wind. This happens because the aerodynamic stress encountered at this point is fairly small due to low values of both Q and α. In fact, for the configurations under analysis, the vehicle can always be trimmed using individual fin or TVC deflections under 1 degree.

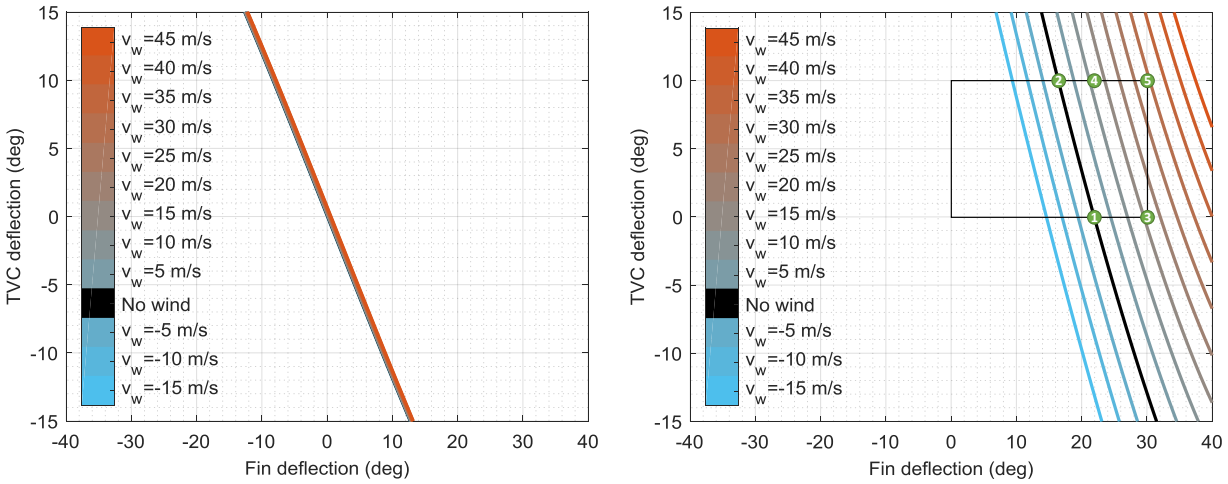

(a) Booster re-ignition (t = 288 s)

(b) Maximum recovery Q_α (t = 335 s)

Fig. 15 Attitude trim curves at extreme flight conditions

This situation is naturally opposed to the point of maximum Q_α, depicted in Fig. 15b. The first conclusion to be drawn from here is that the vehicle could not be controlled without using fins, as the trim curves do not intersect the $\beta_{\text{fin,y}} = 0$ coordinate. In contrast, without using TVC, trim with no wind requires a fin deflection of about 22 deg (point ① in the figure). This equilibrium value is very close to the one observed in Fig. 13 at 335 seconds, where the vehicle is slowly pitching up in preparation for landing. The required fin deflection could however be alleviated for example to 16.4 deg, allowing an additional TVC deflection of 10 deg (point ②).

Introducing wind then makes the vehicle's controllability more challenging. Suppose a maximum authority of 30 deg is allocated to the fins. In case there is wind, fins alone allow to compensate for speeds up to 16 m/s (point ③) or, if they are fixed to their previous value and TVC is used, up to 12 m/s (point ④). However, if an efficient allocation of both fins and TVC is employed, the present configuration allows to accommodate wind speeds of 29 m/s (point ⑤), which represent rather severe gusts.

In addition to wind, controllability is also affected when the vehicle's properties do not match those assumed at design stage. To demonstrate this effect, the previous analysis is repeated considering multiplicative perturbations in the aerodynamic effectiveness of the vehicle and its fins, μ_α and μ_f. These perturbations cover potential mismatches in terms of CP and CG travel, as well as of reference area and load coefficient of the vehicle and fins.

Trim curves at maximum recovery Q_α are now computed for two corner-cases and illustrated in Fig. 16. Figure 16a shows a case where μ_f is 30% lower and μ_α is the same as before, which accounts for a reduced ability of the fins to counteract loads. Figure 16b depicts a configuration with μ_α 30% higher and same μ_f, simulating an increased proneness of the vehicle to generate aerodynamic loads.

As expected, both cases lead to a more challenging controllability of the vehicle, but its attitude trim capability

remains ensured over a very wide range of wind speeds. For instance, with full fin and TVC deflections (point ⑤), the maximum velocity that can be accommodated is reduced from 29 to 25 m/s in the first case and to 23 m/s in the second. Despite being generally verified, this conclusion does not hold for every control combination because, in addition to control effectiveness, fin effectiveness contributes to the vehicle aerodynamics as well (recall the generalisation of $\mu_{\alpha'}$ in Eq. (33)). As an example, the wind velocity tolerated in point ④ increases from 12 m/s in Fig. 15b to 15 m/s in Fig. 16a.

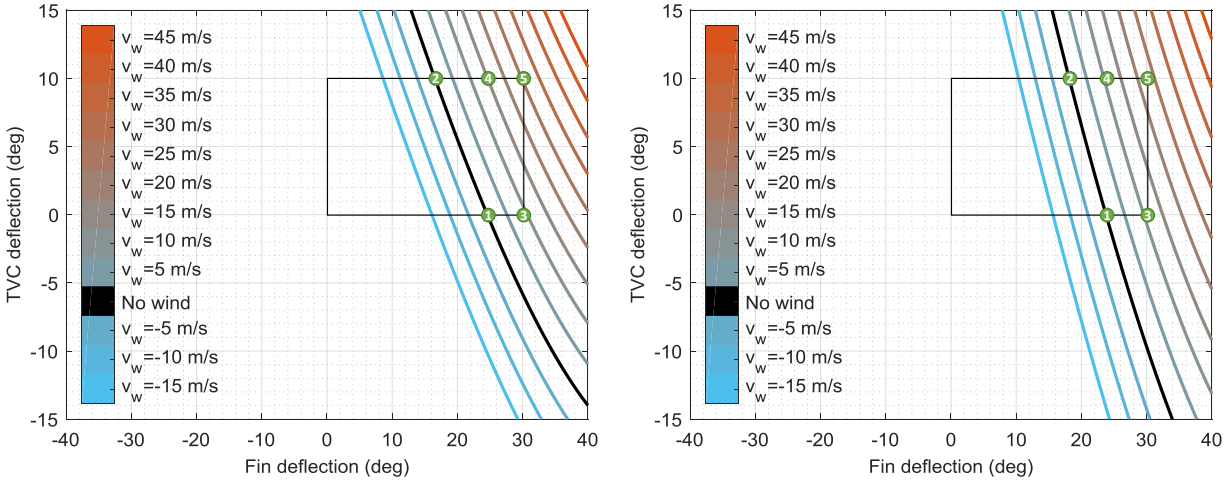

(a) μ_{f} 30% lower (same μ_{α}) (b) μ_{α} 30% higher (same μ_{f})

Fig. 16 Attitude trim curves at maximum recovery Q_{α} with corner-case RLV properties

The control and allocation laws adopted in this study represent a baseline against which more sophisticated techniques will be compared in subsequent works. As mentioned in Sec. IV, attitude control must account for effects such as drift, angle of attack (thus normal load) and wind. The latter, for example, will require specific developments since, as evidenced by the analysis above, extra control moment authority is necessary in addition to the already-demanding fin deflections during descent, which must be efficiently shared between fins and TVC.

VI. Conclusions

The maximisation of reusable launcher flight performance while meeting tight aerodynamic and thermal load constraints is a challenging problem. Significant benefits can be achieved by jointly addressing the two tasks of dimensioning (vehicle and components) and design (guidance and control). But in order to do this, a complete revision of the current process for launchers must be performed to manage the more complex process of reusable launchers.

In this article, a flight mechanics model of a reusable launch vehicle (RLV) has been developed to study and address the critical coupling between guidance and control. It incorporates the main critical components for studying such effects, although some standard simplifying assumptions have been employed. Despite these assumptions, the validity of the benchmark has been verified using standard guidance and control (G&C) designs.

This integrated G&C approach allowed to perform preliminary assessments of different RLV recovery strategies and of the controllability challenges encountered, while highlighting the existing room for improvement. For example, concerning guidance, more powerful approaches based on convex optimisation have shown promise (see [9, 27]), while in terms of control, approaches based on robust algorithms as well as active load prediction and relief schemes are also expected to result in improved designs and mission gains.

Funding Sources

This work is funded by an ESA Networking Partnering Initiative (NPI) contract No. 4000119571/17/NL/MH with Dr. Stephan Theil (DLR-Bremen) as project coordinator. Mr. Simplício is also the recipient of a Doctoral Training Partnership (DTP) award by the UK EPSRC.

Acknowledgements

The authors would like to acknowledge and thank the support and help of Dr. Stephan Theil (DLR-Bremen, Germany) and Christophe Roux (AVIO, Italy).

References

[1] Blackmore, L., "Autonomous Precision Landing of Space Rockets," *The Bridge on Frontiers of Engineering*, Vol. 4, No. 46, 2016, pp. 15–20.

[2] Bradford, J., and Hellman, B., "Return to Launch Site Trajectory Options for a Reusable Booster without a Secondary Propulsion System," *The AIAA SPACE 2009 Conference and Exposition*, Passadena, CA, 2009. doi:10.2514/6.2009-6439.

[3] Bradford, J., Germain, B., and Feld, K., "Optimization of a Reusable Rocket-Powered, VTVL Launch System: A Case Study of the Falcon 9-R," *SpaceWorks Case Study*, 2014.

[4] Tartabini, P., Beaty, J., Lepsch, R., and Gilbert, M., *Payload Performance Analysis for a Reusable Two-Stage-to-Orbit Vehicle*, NASA Technical Reports Server, 2015.

[5] Sippel, M., Stappert, S., Bussler, L., and Dumont, E., "Systematic Assessment of Reusable First-Stage Return Options," *The 68th International Astronautical Congress*, Adelaide, Australia, 2017.

[6] Dumont, E., Stappert, S., Ecker, T., Wilken, J., Karl, S., Krummen, S., and Sippel, M., "Evaluation of Future Ariane Reusable VTOL Booster Stages," *The 68th International Astronautical Congress*, Adelaide, Australia, 2017.

[7] Starr, B., Yunis, I., and Aaron, O., "Use of Flexible Body Coupled Loads in Assessment of Day of Launch Flight Loads," *The 2011 AIAA Atmospheric Flight Mechanics Conference*, Portland, OR, 2011. doi:10.2514/6.2011-6465.

[8] Mooij, E., and Gransden, D., "The Impact of Aeroelastic Effects on the Controllability of Conventional Launch Vehicles," *The 67th International Astronautical Congress*, Guadalajara, Mexico, 2016.

[9] Simplício, P., Marcos, A., and Bennani, S., "Guidance of Reusable Launchers: Improving Descent and Landing Performance," *Journal of Guidance, Control, and Dynamics*, 2019. doi:10.2514/1.G004155, accepted, in press.

[10] Greensite, A. L., *Analysis and Design of Space Vehicle Flight Control Systems*, Vol. II and VII, Spartan, 1970.

[11] Regan, F. J., and Anandakrishnan, S. M., *Dynamics of Atmospheric Re-Entry*, AIAA Education Series, 1993. doi:10.2514/4.861741.

[12] Isakowitz, S., Hopkins Jr., J., and Hopkins, J., *International Reference Guide to Space Launch Systems*, 3rd ed., AIAA, 1999. doi:10.2514/4.475917.

[13] *MATLAB Aerospace Toolbox User's Guide*, 23rd ed., MathWorks, 2017.

[14] Pavlis, N., Holmes, S., Kenyon, S., and Factor, J., "An Earth Gravitational Model to Degree 2160: EGM2008," *The 2008 General Assembly of the European Geosciences Union*, Vienna, Austria, 2008.

[15] *U.S. Standard Atmosphere*, NASA Technical Reports Server, 1976.

[16] Eke, F. O., *Dynamics of Variable Mass Systems*, NASA Technical Reports Server, 1998.

[17] Bianchi, S., "VEGA, the European small launcher: Development status, future perspectives, and applications," *Acta Astronautica*, Vol. 63, 2008, pp. 416–427. doi:10.1016/j.actaastro.2007.12.058.

[18] Ecker, T., Karl, S., Dumont, E., Stappert, S., and Krause, D., "A Numerical Study on the Thermal Loads during a Supersonic Rocket Retro-propulsion Maneuver," *The 53rd AIAA/SAE/ASEE Joint Propulsion Conference*, Atlanta, GA, 2017. doi:10.2514/6.2017-4878.

[19] Chinnery, A., and Shotwell, G., "Space Exploration Technologies' Falcon I Launcher: Towards Operationally Responsive Spacelift," *The 40th AIAA/ASME/SAE/ASEE Joint Propulsion Conference and Exhibit*, Fort Lauderdale, FL, 2004. doi:10.2514/6.2004-3905.

[20] Zarchan, P., *Tactical and Strategic Missile Guidance*, 2nd ed., AIAA Progress in Astronautics and Aeronautics, 1994. doi:10.2514/4.868948.

[21] D'Souza, C., "An optimal guidance law for planetary landing," *The 1997 AIAA Guidance, Navigation, and Control Conference*, New Orleans, LA, 1997. doi:10.2514/6.1997-3709.

[22] Ebrahimi, B., Bahrami, M., and Roshanian, J., "Optimal sliding-mode guidance with terminal velocity constraint for fixed-interval propulsive maneuvers," *Acta Astronautica*, Vol. 62, 2008, pp. 556–562. doi:10.1016/j.actaastro.2008.02.002.

[23] Hawkins, M., Guo, Y., and Wie, B., "Spacecraft Guidance Algorithms for Asteroid Intercept and Rendezvous Missions," *International Journal of Aeronautical and Space Sciences*, Vol. 13, No. 2, 2012, pp. 154–169. doi:10.5139/IJASS.2012.13.2.154.

[24] Guo, Y., Hawkins, M., and Wie, B., "Applications of Generalized Zero-Effort-Miss/Zero-Effort-Velocity Feedback Guidance Algorithm," *Journal of Guidance, Control, and Dynamics*, Vol. 36, No. 3, 2013, pp. 810–820. doi:10.2514/1.58099.

[25] Simplício, P., Marcos, A., Joffre, E., Zamaro, M., and Silva, N., "Parameterised Laws for Robust Guidance and Control of Planetary Landers," *The 4th CEAS EuroGNC Conference*, Warsaw, Poland, 2017.

[26] Joffre, E., Zamaro, M., Silva, N., Marcos, A., and Simplício, P., "Trajectory design and guidance for landing on Phobos," *Acta Astronautica*, Vol. 151, 2018, pp. 389–400. doi:10.1016/j.actaastro.2018.06.024.

[27] Açikmeşe, B., Aung, M., Casoliva, J., Mohan, S., Johnson, A., Scharf, D., Masten, D., Scotkin, A., Wolf, S., and Regehr, M., "Flight Testing of Trajectories Computed by G-FOLD: Fuel Optimal Large Divert Guidance Algorithm for Planetary Landing," *The 23rd AAS/AIAA Spacefilght Mechanics Meeting*, Kauai, HI, 2013.

[28] Knoblauch, M., Saussié, D., and Bérard, C., "Structured H-Infinity Control for a Launch Vehicle," *The 2012 American Control Conference*, Montreal, Canada, 2012. doi:10.1109/ACC.2012.6315181.

[29] Simplício, P., Bennani, S., Marcos, A., Roux, C., and Lefort, X., "Structured Singular-Value Analysis of the Vega Launcher in Atmospheric Flight," *Journal of Guidance, Control, and Dynamics*, Vol. 39, No. 6, 2016, pp. 1342–1355. doi:10.2514/1.G000335.

[30] Navarro-Tapia, D., Marcos, A., Bennani, S., and Roux, C., "Structured H-Infinity Control Based on Classical Control Parameters for the VEGA Launch Vehicle," *The 2016 IEEE Conference on Control Applications*, Buenos Aires, Argentina, 2016. doi:10.1109/CCA.2016.7587818.

[31] Navarro-Tapia, D., Marcos, A., Simplício, P., Bennani, S., and Roux, C., "Legacy Recovery and Robust Augmentation Structured Design for the VEGA Launcher," *International Journal of Robust and Nonlinear Control*, Vol. 29, No. 11, 2019. doi:10.1002/rnc.4557.

[32] Marcos, A., Mostaza, D., and Penin, L., "Achievable Moments NDI-based Fault Tolerant Thrust Vector Control of an Atmospheric Vehicle during Ascent," *The 7th IFAC Symposium on Fault Detection, Supervision and Safety of Technical Processes*, Barcelona, Spain, 2009. doi:10.3182/20090630-4-ES-2003.00103.